



# Novel local characteristic decomposition based path-conservative central-upwind schemes

Shaoshuai Chu<sup>a</sup>, Michael Herty<sup>a</sup>, Alexander Kurganov<sup>b, ,\*</sup>

<sup>a</sup> Department of Mathematics, RWTH Aachen University, Aachen, 52056, Germany

<sup>b</sup> Department of Mathematics, Shenzhen International Center for Mathematics, and Guangdong Provincial Key Laboratory of Computational Science and Material Design, Southern University of Science and Technology, Shenzhen, 518055, China

## ARTICLE INFO

### MSC:

76M12  
65M08  
35L65  
86-08  
76T99

### Keywords:

Local characteristic decomposition  
Path-conservative central-upwind schemes  
Flux globalization  
Compressible multifluids  
Thermal rotating shallow water equations

## ABSTRACT

We introduce local characteristic decomposition based path-conservative central-upwind schemes for (nonconservative) hyperbolic systems of balance laws. The proposed schemes are made to be well-balanced via a flux globalization approach, in which source terms are incorporated into the fluxes: This helps to enforce the well-balanced property when the resulting quasi-conservative system is solved using the local characteristic decomposition based central-upwind scheme recently introduced in [A. CHERTOCK, S. CHU, M. HERTY, A. KURGANOV, AND M. LUKÁČOVÁ-MEDVIĐOVÁ, *J. Comput. Phys.*, 473 (2023), Paper No. 111718]. Nonconservative product terms are also incorporated into the global fluxes using a path-conservative technique. We illustrate the performance of the developed schemes by applying them to one- and two-dimensional compressible multifluid systems and thermal rotating shallow water equations.

## 1. Introduction

This paper is focused on the development of highly accurate and robust numerical methods for the nonconservative hyperbolic systems of balance laws, which in the one-dimensional (1-D) case read as

$$U_t + F(U)_x = B(U)U_x + S(x, t, U), \quad (1.1)$$

where  $x$  is a spatial variable,  $t$  is the time,  $U \in \mathbb{R}^d$  is a vector of unknown functions,  $F : \mathbb{R}^d \rightarrow \mathbb{R}^d$  are nonlinear fluxes,  $B \in \mathbb{R}^{d \times d}$ , and  $S : \mathbb{R}^d \rightarrow \mathbb{R}^d$  are source terms.

Designing a numerical scheme for (1.1) is a challenging task for a number of reasons. First, it is well-known that solutions of (1.1) may develop complicated nonsmooth structures even for smooth initial data. Second, the presence of nonconservative products (when  $B \neq 0$ ) brings many challenges for studying these systems both theoretically and numerically. In general, when  $U$  is discontinuous, weak solutions of (1.1) cannot be understood in the sense of distributions. Instead, one can introduce Borel measure solutions [19,30,31]. This concept of weak solutions was utilized to develop path-conservative finite-volume (FV) methods; see, e.g., [1,6–9,35,36,38]

\* Corresponding author.

E-mail addresses: [chuss2019@mail.sustech.edu.cn](mailto:chuss2019@mail.sustech.edu.cn) (S. Chu), [herty@igpm.rwth-aachen.de](mailto:herty@igpm.rwth-aachen.de) (M. Herty), [alexander@sustech.edu.cn](mailto:alexander@sustech.edu.cn) (A. Kurganov).

<https://doi.org/10.1016/j.jcp.2024.113692>

Received 2 May 2024; Received in revised form 22 November 2024; Accepted 17 December 2024

and reference therein. Third, a novel scheme should be well-balanced (WB) in the sense that it should be capable of exactly preserving some of the physically relevant steady-state solutions satisfying

$$F(U)_x - B(U)U_x - S(x, t, U) = M(U)E(x, t, U)_x = \mathbf{0}.$$

Here,  $M \in \mathbb{R}^{d \times d}$  and  $E$  is the vector of equilibrium variables, which are constant at the steady states provided  $M$  is invertible; see [26]. Particular details of  $M$  and  $E$  depend on the problem at hand.

In this paper, we focus on one of the popular classes of FV methods, the Riemann-problem-solver-free central-upwind (CU) schemes, which were originally introduced in [25,28,29] as a “black-box” solver for general multidimensional hyperbolic systems of conservation laws and then successfully applied to a variety of hyperbolic systems. In [8], the CU schemes were first reformulated in a path-conservative framework and then extended to the 1-D nonconservative systems (1.1), resulting in the second-order path-conservative CU (PCCU) schemes. These schemes are WB in the sense that they are capable of preserving simple steady-state solutions like “lake-at-rest” of several shallow water models.

In order to design PCCU schemes capable of preserving more complicated steady states, path-conservative techniques were incorporated into the flux globalization framework: This results in a new class of flux globalization based WB PCCU schemes introduced in [26]. A flux globalization approach, which was introduced in [5,14,20,21,33], relies on the following quasi-conservative form of (1.1):

$$U_t + K(U)_x = \mathbf{0}, \tag{1.2}$$

where  $K(U)$  is a global flux

$$K(U) = F(U) - W(U), \quad W(U) = \int_{\hat{x}}^x [B(U)U_\xi(\xi, t) + S(\xi, t, U(\xi, t))] d\xi, \tag{1.3}$$

and  $\hat{x}$  is an arbitrary number. The flux globalization based WB PCCU schemes are obtained by applying the CU numerical flux to the semi-discretization of (1.2) and by using the path-conservative technique for the evaluation of the integrals in (1.3). These schemes have been applied to a variety of hyperbolic systems in [2–4,10,17,26].

Even though the flux globalization based WB PCCU schemes from [26] are accurate, efficient, and robust, higher resolution of the numerical solutions can be achieved by reducing numerical dissipation present in those schemes. This can be done, for example, by using the local characteristic decomposition (LCD) based CU (LCD-CU) numerical fluxes instead of the original CU ones employed in [2–4,10,26]. The LCD-CU schemes have been recently introduced in [12] for hyperbolic systems of conservation laws, but its proper extension to the hyperbolic systems of balance laws is not straightforward. In this paper, we use the flux globalization approach and then apply the LCD-CU numerical fluxes to the resulting quasi-conservative systems to substantially enhance the performance of the flux globalization based WB PCCU schemes. Effectively, this approach is equivalent to a very specific discretization of the source and nonconservative product terms, which could be hard to develop without the flux globalization approach, which allows one to “automatically” balance the terms and, at the same time, to use the LCD-based technique to reduce the amount of numerical dissipation present at the Riemann-problem-solver-free (and hence robust) CU numerical fluxes. We derive the new LCD-PCCU schemes and apply them to two particular systems. First, we consider the  $\gamma$ -based compressible multifluid systems, which can be, in principle, written in the conservative form, but we use its nonconservative formulation to achieve high resolution of material interfaces. Second, we consider a challenging thermal rotating shallow water (TRSW) model, which contains geometric source term due to a nonflat bottom topography, source terms due to Coriolis forces, and generically nonconservative momentum exchange terms.

The rest of the paper is organized as follows. In §2, we briefly describe the 1-D second-order LCD-CU scheme. In §3, we propose the novel scheme by considering the nonconservative system (1.1) and design a 1-D flux globalization based WB LCD-PCCU scheme. In §4, we extend the 1-D LCD-PCCU scheme to the two-dimensional (2-D) case. Finally, in §5, we apply the developed LCD-PCCU schemes to the  $\gamma$ -based compressible multifluid systems and TRSW equations. We illustrate the performance of the scheme on a number of numerical examples.

## 2. 1-D LCD-CU scheme

In this section, we briefly describe the second-order semi-discrete LCD-CU scheme, which is a slightly modified version of the scheme from [12]. For the difference between the schemes, we refer the reader to Remarks 2.1–2.3 below.

We consider a 1-D hyperbolic system of conservative laws

$$U_t + F(U)_x = \mathbf{0}, \tag{2.1}$$

cover the computational domain with the uniform cells  $C_j := [x_{j-\frac{1}{2}}, x_{j+\frac{1}{2}}]$  of size  $\Delta x$  centered at  $x_j = (x_{j-\frac{1}{2}} + x_{j+\frac{1}{2}})/2$ , and denote by  $\bar{U}_j(t)$  the computed cell averages of  $U(\cdot, t)$ ,

$$\bar{U}_j(t) \approx \frac{1}{\Delta x} \int_{C_j} U(x, t) dx, \quad j = 1, \dots, N,$$

which are assumed to be available at a certain time  $t \geq 0$ . Note that both  $\bar{U}_j(t)$  and many other indexed quantities below are time-dependent, but from here on, we suppress their time-dependence for the sake of brevity.

The computed cell averages (2.1) are evolved in time by numerically solving the following system of ODEs:

$$\frac{d\bar{U}_j}{dt} = - \frac{\mathcal{F}_{j+\frac{1}{2}}^{\text{LCD}} - \mathcal{F}_{j-\frac{1}{2}}^{\text{LCD}}}{\Delta x},$$

where the LCD-CU numerical fluxes are given by

$$\mathcal{F}_{j+\frac{1}{2}}^{\text{LCD}} = R_{j+\frac{1}{2}} P_{j+\frac{1}{2}}^{\text{LCD}} R_{j+\frac{1}{2}}^{-1} F_{j+\frac{1}{2}}^- + R_{j+\frac{1}{2}} M_{j+\frac{1}{2}}^{\text{LCD}} R_{j+\frac{1}{2}}^{-1} F_{j+\frac{1}{2}}^+ + R_{j+\frac{1}{2}} Q_{j+\frac{1}{2}}^{\text{LCD}} R_{j+\frac{1}{2}}^{-1} (U_{j+\frac{1}{2}}^+ - U_{j+\frac{1}{2}}^-). \tag{2.2}$$

Here,  $F_j^\pm = F(U_j^\pm)$  and  $U_{j+\frac{1}{2}}^\pm$  are the one-sided values of a piecewise linear interpolant

$$\tilde{U}(x) = \bar{U}_j + (U_x)_j(x - x_j), \quad x \in C_j, \tag{2.3}$$

at the cell interface  $x = x_{j+\frac{1}{2}}$ , namely

$$U_{j+\frac{1}{2}}^- = \bar{U}_j + \frac{\Delta x}{2}(U_x)_j, \quad U_{j+\frac{1}{2}}^+ = \bar{U}_{j+1} - \frac{\Delta x}{2}(U_x)_{j+1}. \tag{2.4}$$

In order to ensure the non-oscillatory nature of this reconstruction, we compute the slopes  $(U_x)_j$  in (2.4) using a generalized minmod limiter [32,34,40]:

$$(U_x)_j = \text{minmod} \left( \theta \frac{\bar{U}_j - \bar{U}_{j-1}}{\Delta x}, \frac{\bar{U}_{j+1} - \bar{U}_{j-1}}{2\Delta x}, \theta \frac{\bar{U}_{j+1} - \bar{U}_j}{\Delta x} \right), \quad \theta \in [1, 2], \tag{2.5}$$

applied in the component-wise manner. Here, the minmod function is defined as

$$\text{minmod}(z_1, z_2, \dots) := \begin{cases} \min_j \{z_j\} & \text{if } z_j > 0 \quad \forall j, \\ \max_j \{z_j\} & \text{if } z_j < 0 \quad \forall j, \\ 0 & \text{otherwise,} \end{cases} \tag{2.6}$$

and the parameter  $\theta$  can be used to control the amount of numerical viscosity present in the resulting scheme. We have taken  $\theta = 1.3$  in all of the numerical experiments reported in §5.

The diagonal matrices  $P_{j+\frac{1}{2}}^{\text{LCD}}$ ,  $M_{j+\frac{1}{2}}^{\text{LCD}}$ , and  $Q_{j+\frac{1}{2}}^{\text{LCD}}$  are given by

$$\begin{aligned} P_{j+\frac{1}{2}}^{\text{LCD}} &= \text{diag}((P_1^{\text{LCD}})_{j+\frac{1}{2}}, \dots, (P_d^{\text{LCD}})_{j+\frac{1}{2}}), & M_{j+\frac{1}{2}}^{\text{LCD}} &= \text{diag}((M_1^{\text{LCD}})_{j+\frac{1}{2}}, \dots, (M_d^{\text{LCD}})_{j+\frac{1}{2}}), \\ Q_{j+\frac{1}{2}}^{\text{LCD}} &= \text{diag}((Q_1^{\text{LCD}})_{j+\frac{1}{2}}, \dots, (Q_d^{\text{LCD}})_{j+\frac{1}{2}}) \end{aligned} \tag{2.7}$$

with

$$\begin{aligned} &((P_i^{\text{LCD}})_{j+\frac{1}{2}}, (M_i^{\text{LCD}})_{j+\frac{1}{2}}, (Q_i^{\text{LCD}})_{j+\frac{1}{2}}) \\ &= \begin{cases} \frac{1}{(\lambda_i^+)_{j+\frac{1}{2}} - (\lambda_i^-)_{j+\frac{1}{2}}} \left( (\lambda_i^+)_{j+\frac{1}{2}}, -(\lambda_i^-)_{j+\frac{1}{2}}, (\lambda_i^+)_{j+\frac{1}{2}} (\lambda_i^-)_{j+\frac{1}{2}} \right) & \text{if } (\lambda_i^+)_{j+\frac{1}{2}} - (\lambda_i^-)_{j+\frac{1}{2}} > \epsilon_0, \\ \frac{1}{a_{j+\frac{1}{2}}^+ - a_{j+\frac{1}{2}}^-} \left( a_{j+\frac{1}{2}}^+, -a_{j+\frac{1}{2}}^-, a_{j+\frac{1}{2}}^+ \text{if}(\lambda_i^+)_{j+\frac{1}{2}} - (\lambda_i^-)_{j+\frac{1}{2}} \leq \epsilon_0 \text{ and } a_{j+\frac{1}{2}}^+ - a_{j+\frac{1}{2}}^- > \epsilon_0, \right. \\ \left. \left( \frac{1}{2}, \frac{1}{2}, 0 \right) \right. & \text{if } a_{j+\frac{1}{2}}^+ - a_{j+\frac{1}{2}}^- \leq \epsilon_0, \end{cases} \end{aligned} \tag{2.8}$$

where

$$\begin{aligned} (\lambda_i^+)_{j+\frac{1}{2}} &= \max \left\{ \lambda_i(A(U_{j+\frac{1}{2}}^-)), \lambda_i(A(U_{j+\frac{1}{2}}^+)), 0 \right\}, \\ (\lambda_i^-)_{j+\frac{1}{2}} &= \min \left\{ \lambda_i(A(U_{j+\frac{1}{2}}^-)), \lambda_i(A(U_{j+\frac{1}{2}}^+)), 0 \right\}, \end{aligned} \quad i = 1, \dots, d.$$

Here,  $A(U) = \frac{\partial F}{\partial U}(U)$  is the Jacobian,  $\lambda_1(A(U)) \leq \dots \leq \lambda_d(A(U))$  are its eigenvalues, and the matrices  $R_{j+\frac{1}{2}}$  and  $R_{j+\frac{1}{2}}^{-1}$  are such that  $R_{j+\frac{1}{2}}^{-1} \hat{A}_{j+\frac{1}{2}} R_{j+\frac{1}{2}}$  is diagonal, where  $\hat{A}_{j+\frac{1}{2}} = A(\hat{U}_{j+\frac{1}{2}})$  and  $\hat{U}_{j+\frac{1}{2}}$  is either a simple average  $(\bar{U}_j + \bar{U}_{j+1})/2$  or another type of average

of the  $\bar{U}_j$  and  $\bar{U}_{j+1}$  states. The one-sided local speeds of propagation  $a_{j+\frac{1}{2}}^\pm$  can be estimated using the largest and the smallest eigenvalues of  $A$ , for example, by taking

$$a_{j+\frac{1}{2}}^+ = \max \left\{ \lambda_d(A(U_{j+\frac{1}{2}}^+)), \lambda_d(A(U_{j+\frac{1}{2}}^-)), 0 \right\}, \quad a_{j+\frac{1}{2}}^- = \min \left\{ \lambda_1(A(U_{j+\frac{1}{2}}^+)), \lambda_1(A(U_{j+\frac{1}{2}}^-)), 0 \right\}.$$

Finally,  $\varepsilon_0$  in (2.8) is a very small desingularization constant, which is taken  $\varepsilon_0 = 10^{-18}$  in all of the numerical examples reported in §5.

**Remark 2.1.** The numerical flux (2.2) is identical to the LCD-CU numerical flux in [12], which we have simplified using the fact that

$$P_{j+\frac{1}{2}}^{\text{LCD}} + M_{j+\frac{1}{2}}^{\text{LCD}} = I, \tag{2.9}$$

where  $I$  is the identity matrix.

**Remark 2.2.** We perform a piecewise linear reconstruction for the conservative variables  $U$  rather than the local characteristic variables as it was done in [12]. As no substantial spurious oscillations have been observed in any of the conducted numerical examples, there is no need to switch to the local characteristic variables in this case. This allows the developed scheme to be more efficient than the original LCD-CU scheme from [12].

**Remark 2.3.** The desingularization in (2.8) is performed differently than in [12]. Our numerical experiments indicate that the current desingularization is more robust compared with the previous desingularization strategy.

### 3. 1-D flux globalization based LCD-PCCU scheme

In this section, we propose an extension of the LCD-CU scheme from §2 to the nonconservative system (1.1) and design a 1-D flux globalization based LCD-PCCU scheme.

We apply the LCD-CU scheme to the quasi-conservative system (1.2)–(1.3) to obtain

$$\frac{d\bar{U}_j}{dt} = - \frac{\mathcal{K}_{j+\frac{1}{2}}^{\text{LCD}} - \mathcal{K}_{j-\frac{1}{2}}^{\text{LCD}}}{\Delta x}, \tag{3.1}$$

where the numerical fluxes  $\mathcal{K}_{j+\frac{1}{2}}^{\text{LCD}}$  are given by (compare with (2.2))

$$\mathcal{K}_{j+\frac{1}{2}}^{\text{LCD}} = R_{j+\frac{1}{2}} P_{j+\frac{1}{2}}^{\text{LCD}} R_{j+\frac{1}{2}}^{-1} \mathbf{K}_{j+\frac{1}{2}}^- + R_{j+\frac{1}{2}} M_{j+\frac{1}{2}}^{\text{LCD}} R_{j+\frac{1}{2}}^{-1} \mathbf{K}_{j+\frac{1}{2}}^+ + R_{j+\frac{1}{2}} Q_{j+\frac{1}{2}}^{\text{LCD}} R_{j+\frac{1}{2}}^{-1} (\check{U}_{j+\frac{1}{2}}^+ - \check{U}_{j+\frac{1}{2}}^-). \tag{3.2}$$

Here,  $\mathbf{K}_{j+\frac{1}{2}}^\pm$  are the global fluxes, which are computed as the same as in [3, §2].

The global fluxes  $\mathbf{K}_{j+\frac{1}{2}}^\pm$  are computed using the point values  $U_{j+\frac{1}{2}}^\pm$ , which, in order to ensure the WB property of the resulting scheme, are to be obtained with the help of a piecewise linear reconstruction (2.3)–(2.6) applied to the equilibrium variables  $E$  (instead of  $U$ ):

$$E_{j+\frac{1}{2}}^- = E_j + \frac{\Delta x}{2} (E_x)_j, \quad E_{j+\frac{1}{2}}^+ = E_{j+1} - \frac{\Delta x}{2} (E_x)_{j+1},$$

where  $E_j := E(x_j, t, \bar{U}_j)$ . We then obtain the corresponding values  $U_{j+\frac{1}{2}}^\pm$  by solving the (nonlinear systems of) equations

$$E(x_{j+\frac{1}{2}} + 0, t, U_{j+\frac{1}{2}}^+) = E_{j+\frac{1}{2}}^+ \quad \text{and} \quad E(x_{j+\frac{1}{2}} - 0, t, U_{j+\frac{1}{2}}^-) = E_{j+\frac{1}{2}}^- \tag{3.3}$$

for  $U_{j+\frac{1}{2}}^+$  and  $U_{j+\frac{1}{2}}^-$ , respectively. We emphasize that the values  $U_{j+\frac{1}{2}}^\pm$  cannot be used in (3.2) instead of  $\check{U}_{j+\frac{1}{2}}^\pm$  as  $U_{j+\frac{1}{2}}^+$  may not be equal to  $U_{j+\frac{1}{2}}^-$  at discrete steady states. We therefore use another set of point values  $\check{U}_{j+\frac{1}{2}}^\pm$ , which are obtained by solving modified versions of (3.3):

$$\check{E}(x_{j+\frac{1}{2}} + 0, t, \check{U}_{j+\frac{1}{2}}^+) = E_{j+\frac{1}{2}}^+ \quad \text{and} \quad \check{E}(x_{j+\frac{1}{2}} - 0, t, \check{U}_{j+\frac{1}{2}}^-) = E_{j+\frac{1}{2}}^-.$$

Here, the functions  $\check{E}$  are the modifications of the functions  $E$ , which are made in such a way that  $\check{U}_{j+\frac{1}{2}}^+ = \check{U}_{j+\frac{1}{2}}^-$  as long as  $E_{j+\frac{1}{2}}^+ = E_{j+\frac{1}{2}}^-$  and, at the same time,  $\check{U}_{j+\frac{1}{2}}^+ = U_{j+\frac{1}{2}}^+ + \mathcal{O}((\Delta x)^2)$  and  $\check{U}_{j+\frac{1}{2}}^- = U_{j+\frac{1}{2}}^- + \mathcal{O}((\Delta x)^2)$  for smooth solutions; see [2–4, 10, 26] for examples of such modifications for several particular systems.

The diagonal matrices  $P_{j+\frac{1}{2}}^{\text{LCD}}$ ,  $M_{j+\frac{1}{2}}^{\text{LCD}}$ , and  $Q_{j+\frac{1}{2}}^{\text{LCD}}$  in (3.2) are defined by (2.7)–(2.8), but with

$$\begin{aligned} (\lambda_i^+)_{j+\frac{1}{2}} &= \max \left\{ \lambda_i(\mathcal{A}(U_{j+\frac{1}{2}}^-)), \lambda_i(\mathcal{A}(U_{j+\frac{1}{2}}^+)), 0 \right\}, \\ (\lambda_i^-)_{j+\frac{1}{2}} &= \min \left\{ \lambda_i(\mathcal{A}(U_{j+\frac{1}{2}}^-)), \lambda_i(\mathcal{A}(U_{j+\frac{1}{2}}^+)), 0 \right\}, \end{aligned} \quad i = 1, \dots, d,$$

where  $\mathcal{A}(U) = \frac{\partial F}{\partial U}(U) - B(U)$  and the matrices  $R_{j+\frac{1}{2}}$  and  $R_{j+\frac{1}{2}}^{-1}$  are such that  $R_{j+\frac{1}{2}}^{-1} \hat{\mathcal{A}}_{j+\frac{1}{2}} R_{j+\frac{1}{2}}$  is diagonal for  $\hat{\mathcal{A}}_{j+\frac{1}{2}} = \mathcal{A}(\hat{U}_{j+\frac{1}{2}})$ . Finally, the one-sided local speeds of propagation  $a_{j+\frac{1}{2}}^\pm$  are estimated by

$$a_{j+\frac{1}{2}}^+ = \max \left\{ \lambda_d(\mathcal{A}(U_{j+\frac{1}{2}}^+)), \lambda_d(\mathcal{A}(U_{j+\frac{1}{2}}^-)), 0 \right\}, \quad a_{j+\frac{1}{2}}^- = \min \left\{ \lambda_1(\mathcal{A}(U_{j+\frac{1}{2}}^+)), \lambda_1(\mathcal{A}(U_{j+\frac{1}{2}}^-)), 0 \right\}.$$

**Remark 3.1.** The introduced 1-D semi-discrete flux globalization based LCD-PCCU scheme is WB. In order to prove this, we only need to show that if the discrete data are at a steady state, namely, if  $E_j \equiv \hat{E} = \text{Const}$ , then the RHS of (3.1) vanishes. Following the proof of [3, Theorem 2.1], we obtain

$$K_{j+\frac{1}{2}}^+ = K_{j+\frac{1}{2}}^- = K_{j-\frac{1}{2}}^+ = \hat{K} = \text{Const}, \quad \forall j. \tag{3.4}$$

Substituting (3.4) and (2.9) into (3.2) and taking into account the fact that at the steady states  $\check{U}_{j+\frac{1}{2}}^+ = \check{U}_{j+\frac{1}{2}}^- = \check{U}_{j+\frac{1}{2}}$ ,  $\forall j$ , yields

$$\mathcal{K}_{j+\frac{1}{2}}^{\text{LCD}} = \hat{K} + R_{j+\frac{1}{2}} Q_{j+\frac{1}{2}}^{\text{LCD}} R_{j+\frac{1}{2}}^{-1} (\check{U}_{j+\frac{1}{2}}^+ - \check{U}_{j+\frac{1}{2}}^-) = \hat{K}, \quad \forall j,$$

which ensures that the RHS of (3.1) vanishes.

#### 4. 2-D flux globalization based LCD-PCCU scheme

In this section, we propose a novel 2-D LCD-PCCU scheme for

$$U_t + F(U)_x + G(U)_y = B(U)U_x + C(U)U_y + S^x(x, y, t, U) + S^y(x, y, t, U), \tag{4.1}$$

where  $F, G : \mathbb{R}^d \rightarrow \mathbb{R}^d$ ,  $B, C \in \mathbb{R}^{d \times d}$ ,  $S^x : \mathbb{R}^d \rightarrow \mathbb{R}^d$ , and  $S^y : \mathbb{R}^d \rightarrow \mathbb{R}^d$ . To this end, we design the 2-D scheme in a ‘‘dimension-by-dimension’’ manner.

As in the 1-D case, we first rewrite the general 2-D nonconservative system (4.1) in the following quasi-conservative form:

$$U_t + K(U)_x + L(U)_y = 0, \quad K(U) = F(U) - W^x(U), \quad L(U) = G(U) - W^y(U), \tag{4.2}$$

where

$$\begin{aligned} W^x(U) &:= \int_{\hat{x}}^x [B(U)U_\xi(\xi, y, t) + S^x(\xi, y, t, U(\xi, y, t))] d\xi, \\ W^y(U) &:= \int_{\hat{y}}^y [C(U)U_\eta(x, \eta, t) + S^y(x, \eta, t, U(x, \eta, t))] d\eta, \end{aligned}$$

with  $\hat{x}$  and  $\hat{y}$  being arbitrary numbers.

Applying the 2-D version of the semi-discrete LCD-CU scheme from §2 to the quasi-conservative system (4.2) results in the following system of ODEs:

$$\frac{d\bar{U}_{j,k}}{dt} = - \frac{\mathcal{K}_{j+\frac{1}{2},k}^{\text{LCD}} - \mathcal{K}_{j-\frac{1}{2},k}^{\text{LCD}}}{\Delta x} - \frac{\mathcal{L}_{j,k+\frac{1}{2}}^{\text{LCD}} - \mathcal{L}_{j,k-\frac{1}{2}}^{\text{LCD}}}{\Delta y}, \tag{4.3}$$

where the numerical fluxes  $\mathcal{K}_{j+\frac{1}{2},k}^{\text{LCD}}$  and  $\mathcal{L}_{j,k+\frac{1}{2}}^{\text{LCD}}$  are given by

$$\begin{aligned}
 \mathcal{K}_{j+\frac{1}{2},k}^{\text{LCD}} &= R_{j+\frac{1}{2},k} P_{j+\frac{1}{2},k}^{\text{LCD}} R_{j+\frac{1}{2},k}^{-1} \mathbf{K}(U_{j,k}^{\text{E}}) + R_{j+\frac{1}{2},k} M_{j+\frac{1}{2},k}^{\text{LCD}} R_{j+\frac{1}{2},k}^{-1} \mathbf{K}(U_{j+1,k}^{\text{W}}) \\
 &\quad + R_{j+\frac{1}{2},k} Q_{j+\frac{1}{2},k}^{\text{LCD}} R_{j+\frac{1}{2},k}^{-1} (\check{U}_{j+1,k}^{\text{W}} - \check{U}_{j,k}^{\text{E}}), \\
 \mathcal{L}_{j,k+\frac{1}{2}}^{\text{LCD}} &= R_{j,k+\frac{1}{2}} P_{j,k+\frac{1}{2}}^{\text{LCD}} R_{j,k+\frac{1}{2}}^{-1} \mathbf{L}(U_{j,k}^{\text{N}}) + R_{j,k+\frac{1}{2}} M_{j,k+\frac{1}{2}}^{\text{LCD}} R_{j,k+\frac{1}{2}}^{-1} \mathbf{L}(U_{j,k+1}^{\text{S}}) \\
 &\quad + R_{j,k+\frac{1}{2}} Q_{j,k+\frac{1}{2}}^{\text{LCD}} R_{j,k+\frac{1}{2}}^{-1} (\check{U}_{j,k+1}^{\text{S}} - \check{U}_{j,k}^{\text{N}}).
 \end{aligned} \tag{4.4}$$

Here,  $\mathbf{K}(U_{j,k}^{\text{E}})$ ,  $\mathbf{K}(U_{j+1,k}^{\text{W}})$  and  $\mathbf{L}(U_{j,k}^{\text{N}})$ ,  $\mathbf{L}(U_{j,k+1}^{\text{S}})$  are global fluxes in the  $x$ - and  $y$ -direction, computed using the corresponding reconstructed point values

$$\begin{aligned}
 U_{j,k}^{\text{E}} &\approx U(x_{j+\frac{1}{2}} - 0, y_k, t), & U_{j+1,k}^{\text{W}} &\approx U(x_{j+\frac{1}{2}} + 0, y_k, t), \\
 U_{j,k}^{\text{N}} &\approx U(x_j, y_{k+\frac{1}{2}} - 0, t), & U_{j,k+1}^{\text{S}} &\approx U(x_j, y_{k+\frac{1}{2}} + 0, t),
 \end{aligned}$$

$\check{U}_{j,k}^{\text{E}}$ ,  $\check{U}_{j+1,k}^{\text{W}}$ ,  $\check{U}_{j,k}^{\text{N}}$  and  $\check{U}_{j,k+1}^{\text{S}}$  are alternative approximations of the same point values, and the matrices  $P_{j+\frac{1}{2},k}^{\text{LCD}}$ ,  $P_{j,k+\frac{1}{2}}^{\text{LCD}}$ ,  $M_{j+\frac{1}{2},k}^{\text{LCD}}$ ,  $M_{j,k+\frac{1}{2}}^{\text{LCD}}$ ,  $Q_{j+\frac{1}{2},k}^{\text{LCD}}$  and  $Q_{j,k+\frac{1}{2}}^{\text{LCD}}$  are analogous to the corresponding matrices  $P_{j+\frac{1}{2}}^{\text{LCD}}$ ,  $M_{j+\frac{1}{2}}^{\text{LCD}}$ , and  $Q_{j+\frac{1}{2}}^{\text{LCD}}$  in the 1-D case.

For details on the evaluation of the point values of  $U$ , we refer the reader to [2]. The global fluxes  $\mathbf{K}(U_{j,k}^{\text{E}})$ ,  $\mathbf{K}(U_{j+1,k}^{\text{W}})$ ,  $\mathbf{L}(U_{j,k}^{\text{N}})$ , and  $\mathbf{L}(U_{j,k+1}^{\text{S}})$  are computed using the WB path-conservative technique as in [2]. The LCD matrices  $P_{j+\frac{1}{2},k}^{\text{LCD}}$ ,  $M_{j+\frac{1}{2},k}^{\text{LCD}}$ ,  $Q_{j+\frac{1}{2},k}^{\text{LCD}}$ ,  $P_{j,k+\frac{1}{2}}^{\text{LCD}}$ ,  $M_{j,k+\frac{1}{2}}^{\text{LCD}}$ , and  $Q_{j,k+\frac{1}{2}}^{\text{LCD}}$  are computed as in [12], but based on the eigensystems of  $\hat{A}_{j+\frac{1}{2},k}^{\text{F}} = \mathcal{A}^{\text{F}}(\hat{U}_{j+\frac{1}{2},k}) := \frac{\partial \mathcal{F}}{\partial U}(\hat{U}_{j+\frac{1}{2},k}) - \mathcal{B}(\hat{U}_{j+\frac{1}{2},k})$  and  $\hat{A}_{j,k+\frac{1}{2}}^{\text{G}} = \mathcal{A}^{\text{G}}(\hat{U}_{j,k+\frac{1}{2}}) := \frac{\partial \mathcal{G}}{\partial U}(\hat{U}_{j,k+\frac{1}{2}}) - \mathcal{C}(\hat{U}_{j,k+\frac{1}{2}})$ , where  $\hat{U}_{j+\frac{1}{2},k}$  is a proper average of  $\bar{U}_{j+1,k}$  and  $\bar{U}_{j,k}$ , and  $\hat{U}_{j,k+\frac{1}{2}}$  is a proper average of  $\bar{U}_{j,k+1}$  and  $\bar{U}_{j,k}$ . As in §2, we do not employ local characteristic variables in the piecewise linear reconstruction and perform the desingularization of  $P_{j+\frac{1}{2},k}^{\text{LCD}}$ ,  $M_{j+\frac{1}{2},k}^{\text{LCD}}$ ,  $Q_{j+\frac{1}{2},k}^{\text{LCD}}$ ,  $P_{j,k+\frac{1}{2}}^{\text{LCD}}$ ,  $M_{j,k+\frac{1}{2}}^{\text{LCD}}$ , and  $Q_{j,k+\frac{1}{2}}^{\text{LCD}}$  as in (2.8).

**Remark 4.1.** The introduced 2-D semi-discrete flux globalization based LCD-PCCU scheme is WB in the sense that it is capable of exactly preserving discrete steady states, for which  $\mathbf{K}(U)$  is independent of  $x$  and  $\mathbf{L}(U)$  is independent of  $y$ . We omit the proof for the sake of brevity. We stress that the 2-D systems may admit genuinely 2-D steady states, which cannot be preserved by the proposed scheme. To the best of our knowledge, no existing numerical method is capable of exactly preserving general 2-D steady states, even the smooth ones.

### 5. Numerical examples

In this section, we apply the developed LCD-PCCU schemes to the  $\gamma$ -based compressible multifluid and TRSW equations. We conduct several numerical experiments and compare the performance of the LCD-PCCU schemes with their PCCU counterparts obtained by applying the original CU numerical fluxes in (3.1) and (4.3). For instance, in the 1-D case, such a PCCU scheme is obtained by replacing (2.8) by

$$((P_i)_{j+\frac{1}{2}}, (M_i)_{j+\frac{1}{2}}, (Q_i)_{j+\frac{1}{2}}) = \begin{cases} \left( \frac{1}{a_{j+\frac{1}{2}}^+ - a_{j+\frac{1}{2}}^-} (a_{j+\frac{1}{2}}^+, -a_{j+\frac{1}{2}}^-, a_{j+\frac{1}{2}}^+, a_{j+\frac{1}{2}}^-) \right) & \text{if } a_{j+\frac{1}{2}}^+ - a_{j+\frac{1}{2}}^- > \epsilon_0, \\ \left( \frac{1}{2}, \frac{1}{2}, 0 \right) & \text{otherwise.} \end{cases}$$

In all of the numerical examples, we have solved the ODE systems (3.1) and (4.3) using the three-stage third-order strong stability preserving (SSP) Runge-Kutta method (see, e.g., [22,23]) and used the CFL number 0.45.

#### 5.1. $\gamma$ -based compressible multifluid equations

In this section, we show the applications of the developed LCD-PCCU schemes introduced in §3 and §4 to the 1-D and 2-D  $\gamma$ -based compressible multifluid systems [11,39], which in the 2-D case can be written as (4.1) with  $U = (\rho, \rho u, \rho v, E, \Gamma, \Pi)^\top$ ,  $F(U) = (\rho u, \rho u^2 + p, \rho uv, u(E + p), 0, 0)^\top$ ,  $G(U) = (\rho v, \rho uv, \rho v^2 + p, v(E + p), 0, 0)^\top$ ,  $S^x(x, y, t, U) = S^y(x, y, t, U) \equiv \mathbf{0}$ ,  $B(U) = \text{diag}(0, 0, 0, 0, u, u)$ , and  $C(U) = \text{diag}(0, 0, 0, 0, v, v)$ . Here,  $\rho$  is the density,  $u$  and  $v$  are the  $x$ - and  $y$ -velocities,  $p$  is the pressure, and  $E$  is the total energy. The system is closed through the following (stiff) equation of state (EOS) for each of the fluid components:

$$p = (\gamma - 1) \left[ E - \frac{\rho}{2}(u^2 + v^2) \right] - \gamma \pi_\infty, \tag{5.1}$$

**Table 5.1**

Example 1:  $L^1$ -errors in  $\rho$  computed by the PCCU and LCD-PCCU schemes and the corresponding experimental convergence rates.

	$\Delta x = 1/50$	$\Delta x = 1/100$	Rate	$\Delta x = 1/200$	Rate
PCCU	1.16e-0	6.65e-1	0.803	3.39e-1	0.972
LCD-PCCU	8.53e-1	4.21e-1	1.019	1.96e-1	1.103

where the parameters  $\gamma$  and  $\pi_\infty$  represent the specific heat ratio and stiffness parameter, respectively (when  $\pi_\infty \equiv 0$  for all of the components, the system reduces to the ideal gas multicomponent case). The variables  $\Gamma$  and  $\Pi$  are defined as  $\Gamma := \frac{1}{\gamma-1}$  and  $\Pi := \frac{\gamma\pi_\infty}{\gamma-1}$ .

**Remark 5.1.** We note that the studied  $\gamma$ -based compressible multifluid equations contain no source terms and thus there is no need to numerically enforce the WB property. We therefore do not need to introduce any equilibrium variables—instead, we reconstruct the conservative quantities  $U$  and replace  $\check{U}_{j+\frac{1}{2}}^\pm$  in (3.2) with  $U_{j+\frac{1}{2}}^\pm$  and  $\check{U}_{j,k}^E, \check{U}_{j+1,k}^W, \check{U}_{j,k}^N$ , and  $\check{U}_{j,k+1}^S$  in (4.4) with  $U_{j,k}^E, U_{j+1,k}^W, U_{j,k}^N$ , and  $U_{j,k+1}^S$ .

**Remark 5.2.** It should be observed that the studied  $\gamma$ -based compressible multifluid system can be rewritten in a fully conservative form by replacing the equation

$$\Gamma_t = -u\Gamma_x - v\Gamma_y \quad \text{and} \quad \Pi_t = -u\Pi_x - v\Pi_y \tag{5.2}$$

with the conservative ones, obtained by combining (5.2) with the continuity equation  $\rho_t + (\rho u)_x + (\rho v)_y = 0$ , which results in

$$(\rho\Gamma)_t + (\rho u\Gamma)_x + (\rho v\Gamma)_y = 0 \quad \text{and} \quad (\rho\Pi)_t + (\rho u\Pi)_x + (\rho v\Pi)_y = 0.$$

However, applying the LCD-CU scheme to the resulting fully conservative system may lead to appearance of significant spurious oscillations in the velocity and pressure fields in the vicinity of contact waves/material interfaces; see [39], where it was shown that a nonconservative form is preferable for designing accurate numerical methods. We therefore solve the nonconservative system, for which, as one can easily prove, the LCD-PPCU schemes satisfy Abgrall’s principle (also called E-property), that is,  $u, v$ , and  $p$  remain constant in the vicinity of isolated contact waves.

**Remark 5.3.** In Appendix A, we provide the expressions for the matrices  $\hat{\mathcal{A}}_{j+\frac{1}{2}}$  and  $\hat{\mathcal{A}}_{j+\frac{1}{2},k}^F$  and the corresponding matrices  $R_{j+\frac{1}{2}}$  and  $R_{j+\frac{1}{2},k}$  for the 1-D and 2-D  $\gamma$ -based compressible multifluid systems, respectively. The matrices  $\hat{\mathcal{A}}_{j,k+\frac{1}{2}}^G$  and  $R_{j,k+\frac{1}{2}}$  can be obtained in an analogous way.

5.1.1. One-dimensional examples

In this section, we consider two numerical examples for the 1-D version of the  $\gamma$ -based compressible multifluid equations.

Example 1—“shock-bubble” interaction

In the first example taken from [18], we consider the “shock-bubble” interaction problem. The initial data are given by

$$(\rho, u, p; \gamma, \pi_\infty)(x, 0) = \begin{cases} (13.1538, 0; 1, 5/3, 0), & |x| < 0.25, \\ (1.3333, -0.3535, 1.5; 1.4, 0), & x > 0.75, \\ (1, 0, 1; 1.4, 0), & \text{otherwise,} \end{cases}$$

which correspond to a left-moving shock, initially located at  $x = 0.75$ , and a resting “bubble” with a radius of 0.25, initially located at the origin.

We impose the solid wall boundary conditions at the both ends of the computational domain  $[-1, 2]$  and compute the numerical solutions by both the LCD-PCCU and PCCU schemes until the final time  $t = 3$  on a uniform mesh with  $\Delta x = 1/50$ . The obtained densities are presented in Fig. 5.1 together with the reference solution computed by the PCCU scheme on a much finer mesh with  $\Delta x = 1/1000$ . As one can see, the LCD-PCCU scheme achieves sharper resolution than the PCCU one. We also compute the  $L^1$ -errors (against the reference solution) in  $\rho$  computed by the PCCU and LCD-PCCU schemes. The errors reported in Table 5.1, confirm that the LCD-PCCU scheme is more accurate than its PCCU counterpart though the experimental convergence rates for both schemes are close to 1 as expected in the case of discontinuous solutions.

Example 2—water-air “shock-bubble” interaction

In the second 1-D example also taken from [18], we consider a gas-liquid multifluid system, where the liquid component is modeled by the stiff EOS (5.1) with  $\pi_\infty \gg 1$ . The initial conditions,

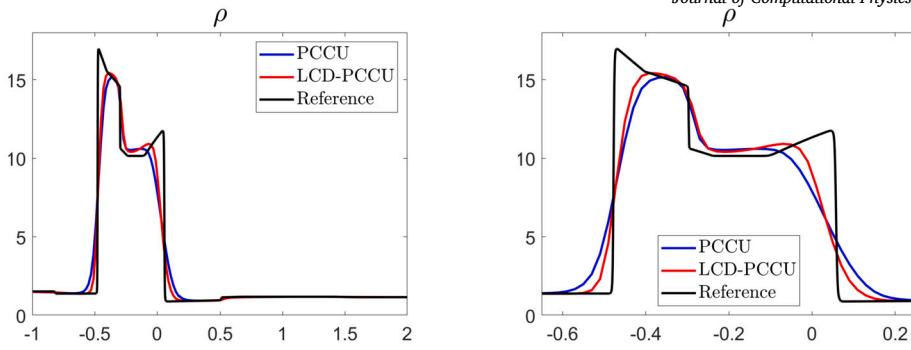


Fig. 5.1. Example 1: Density  $\rho$  computed by the PCCU and LCD-PCCU schemes (left) and zoom at  $x \in [-0.65, 0.25]$  (right). (For interpretation of the colors in the figure(s), the reader is referred to the web version of this article.)

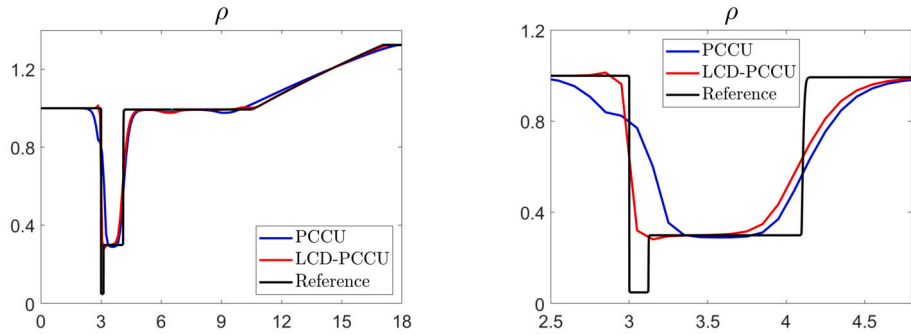


Fig. 5.2. Example 2: Density  $\rho$  computed by the PCCU and LCD-PCCU schemes (left) and zoom at  $x \in [2.5, 4.8]$  (right).

Table 5.2

Example 2:  $L^1$ -errors in  $\rho$  computed by the PCCU and LCD-PCCU schemes and the corresponding experimental convergence rates.

	$\Delta x = 1/10$	$\Delta x = 1/20$	Rate	$\Delta x = 1/40$	Rate
PCCU	4.06e-1	2.57e-1	0.660	1.53e-1	0.748
LCD-PCCU	1.93e-1	1.05e-1	0.878	5.70e-2	0.881

$$(\rho, u, p; \gamma, \pi_\infty) = \begin{cases} (0.05, 0, 1; 1.4, 0), & |x - 6| < 3, \\ (1.325, -68.525, 19153; 4.4, 6000), & x > 11.4, \\ (1, 0, 1; 4.4, 6000), & \text{otherwise,} \end{cases}$$

correspond to the left-moving shock, initially located at  $x = 11.4$ , and a resting air “bubble” with a radius 3, initially located at  $x = 6$ .

We impose the free boundary conditions at the both ends of the computational domain  $[0, 18]$  and compute the numerical solutions until the final time  $t = 0.045$  on a uniform mesh with  $\Delta x = 1/10$  by both the LCD-PCCU and PCCU schemes. The obtained results are presented in Fig. 5.2 together with the reference solution computed by the PCCU scheme on a much finer mesh with  $\Delta x = 1/1000$ . As one can see, the LCD-PCCU solution achieves sharper resolution than its PCCU counterpart, especially of the contact wave located at about  $x = 3$ . In this example, we also compute the  $L^1$ -errors (against the reference solution) in  $\rho$  computed by the PCCU and LCD-PCCU schemes. The errors reported in Table 5.2, show that the LCD-PCCU scheme is more accurate than its PCCU counterpart.

### 5.1.2. Two-dimensional examples

We now consider three 2-D examples, in which we plot the Schlieren images of the magnitude of the density gradient field,  $|\nabla \rho|$ . To this end, we use the shading function

$$\exp\left(-\frac{80|\nabla \rho|}{\max(|\nabla \rho|)}\right),$$

where the numerical derivatives of the density are computed using standard central differencing.

#### Example 3—shock-helium bubble interaction

In the first 2-D example taken from [15,37], a shock wave in the air hits the light resting bubble which contains helium. We take the following initial conditions:

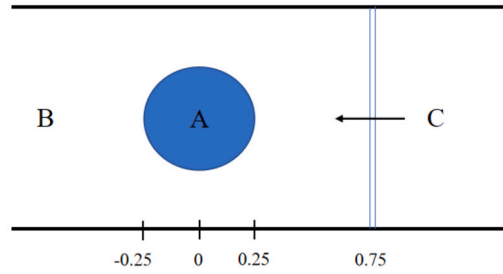


Fig. 5.3. Initial setting for the 2-D numerical examples.

$$(\rho, u, v, p; \gamma, p_\infty) = \begin{cases} (4/29, 0, 0, 1; 5/3, 0) & \text{in region A,} \\ (1, 0, 0, 1; 1.4, 0) & \text{in region B,} \\ (4/3, -0.3535, 0, 1.5; 1.4, 0) & \text{in region C,} \end{cases}$$

where regions A, B, and C are outlined in Fig. 5.3, and the computational domain is  $[-3, 1] \times [-0.5, 0.5]$ . We impose the solid wall boundary conditions on the top and bottom and the free boundary conditions on the left and right edges of the computational domain.

We compute the numerical solutions until the final time  $t = 3$  on a uniform mesh with  $\Delta x = \Delta y = 1/500$ . In Fig. 5.4, we present different stages of the shock-bubble interaction computed by the PCCU and LCD-PCCU schemes. One can clearly see that the bubble interface develops very complex structures after the bubble is hit by the shock, especially at large times. We note that the obtained results are in a good agreement with the experimental findings presented in [24] and the computational results presented in [13, 15, 37]. Notably, at an early time  $t = 0.5$ , the resolution of the bubble interface significantly improves with the implementation of the LCD-PCCU scheme. As time progresses, instabilities arise within the interface, which are smeared by a more dissipative PCCU scheme. The differences in resolution become more pronounced at later times  $t = 2$  and  $2.5$ , and especially at  $t = 3$ , indicating that the LCD-PCCU scheme clearly outperforms the PCCU one.

#### Example 4—shock-R22 bubble interaction

In the second 2-D example also taken from [15, 37], a shock wave in the air hits the heavy resting bubble which contains R22 gas. The initial conditions are

$$(\rho, u, v, p; \gamma, \pi_\infty) = \begin{cases} (3.1538, 0, 0, 1; 1.249, 0) & \text{in region A,} \\ (1, 0, 0, 1; 1.4, 0) & \text{in region B,} \\ (4/3, -0.3535, 0, 1.5; 1.4, 0) & \text{in region C,} \end{cases}$$

and the rest of the settings are the same as in Example 3.

We compute the numerical solutions until the final time  $t = 3$  on a uniform mesh with  $\Delta x = \Delta y = 1/500$  and present different stages of the shock-bubble interaction computed by the PCCU and LCD-PCCU schemes in Fig. 5.5. One can clearly see that upon encountering the bubble, the shock wave undergoes both refraction and reflection. Under the force of the shock, the bubble undergoes compression and motion. These findings are in a good agreement with the computational results reported in [15, 37]. Fig. 5.5 demonstrates that the LCD-PCCU scheme captures material interfaces more accurately (compared to the PCCU scheme) and also enhances the resolution of fine details of the computed solution. Once again, this indicates that the LCD-PCCU scheme is less diffusive than its PCCU counterpart.

#### Example 5—a cylindrical explosion problem

In the last 2-D example taken from [18] (see also [41]), we consider the case where a cylindrical explosive source is located between an air-water interface and an impermeable wall. The initial conditions are given by

$$(\rho, u, v, p; \gamma, \pi_\infty) = \begin{cases} (1.27, 0, 0, 8290, 2, 0), & (x-5)^2 + (y-2)^2 < 1, \\ (0.02, 0, 0, 1; 1.4, 0), & y > 4, \\ (1, 0, 0, 1; 7.15, 3309), & \text{otherwise,} \end{cases}$$

with the solid wall boundary conditions imposed at the bottom, and the free boundary conditions set on the other sides of the computational domain  $[0, 10] \times [0, 6]$ .

We compute the numerical solutions until the final time  $t = 0.02$  on a uniform mesh with  $\Delta x = \Delta y = 1/80$  by the studied PCCU and LCD-PCCU schemes. In Fig. 5.6, we present time snapshots of the obtained results, which qualitatively look similar to the numerical results reported in [18, 41]. As one can see, the LCD-PCCU scheme captures both the material interfaces and many of the developed wave structures substantially sharper than the PCCU scheme.

One can also notice a substantial difference between the PCCU and LCD-PCCU solutions at the final time. In order to clarify this point, we refine the mesh and compute the numerical solution on a finer mesh with  $\Delta x = \Delta y = 1/160$  by the PCCU scheme and

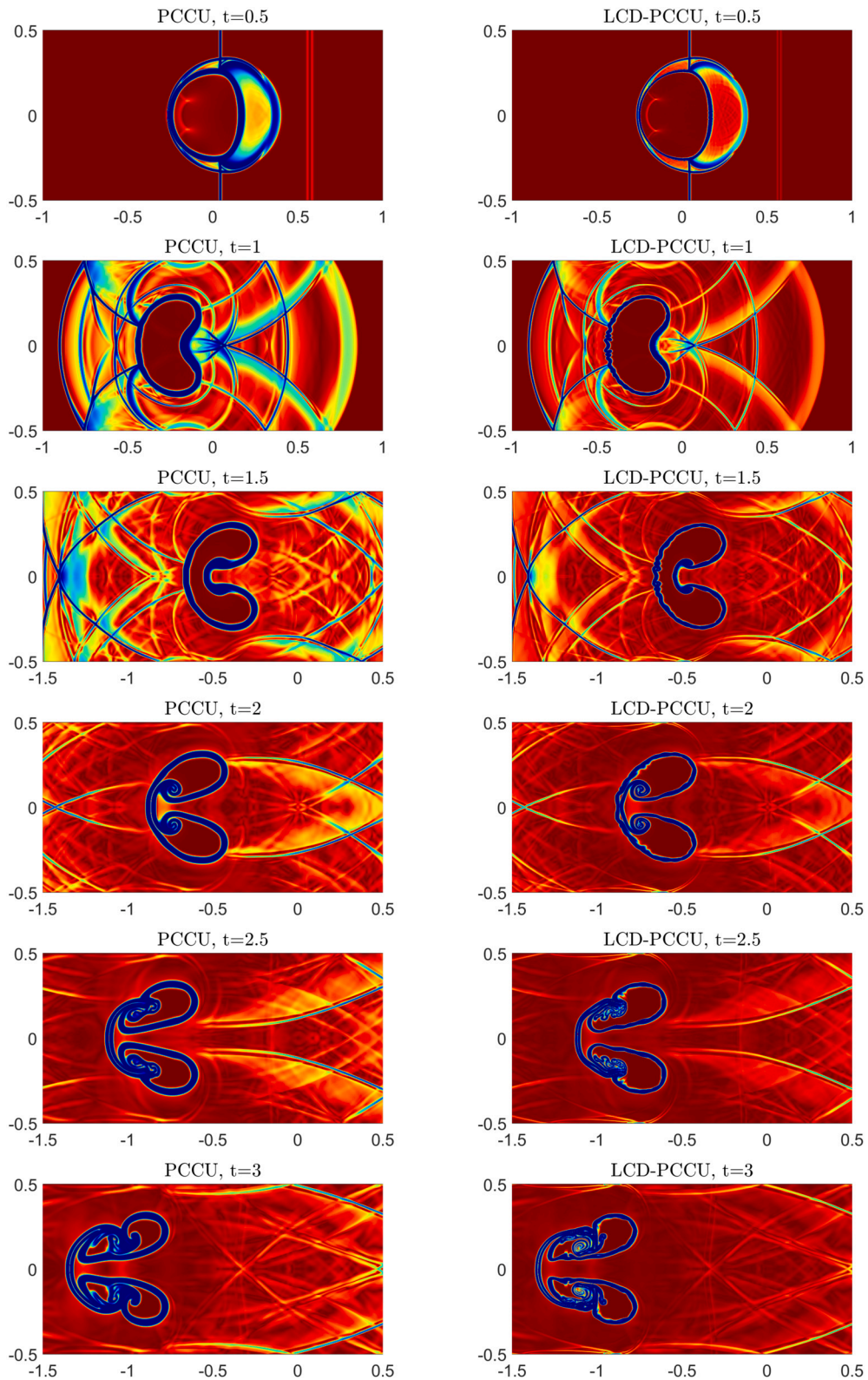


Fig. 5.4. Example 3: Shock-helium bubble interaction by the PCCU (left column) and LCD-PCCU (right column) schemes at different times.

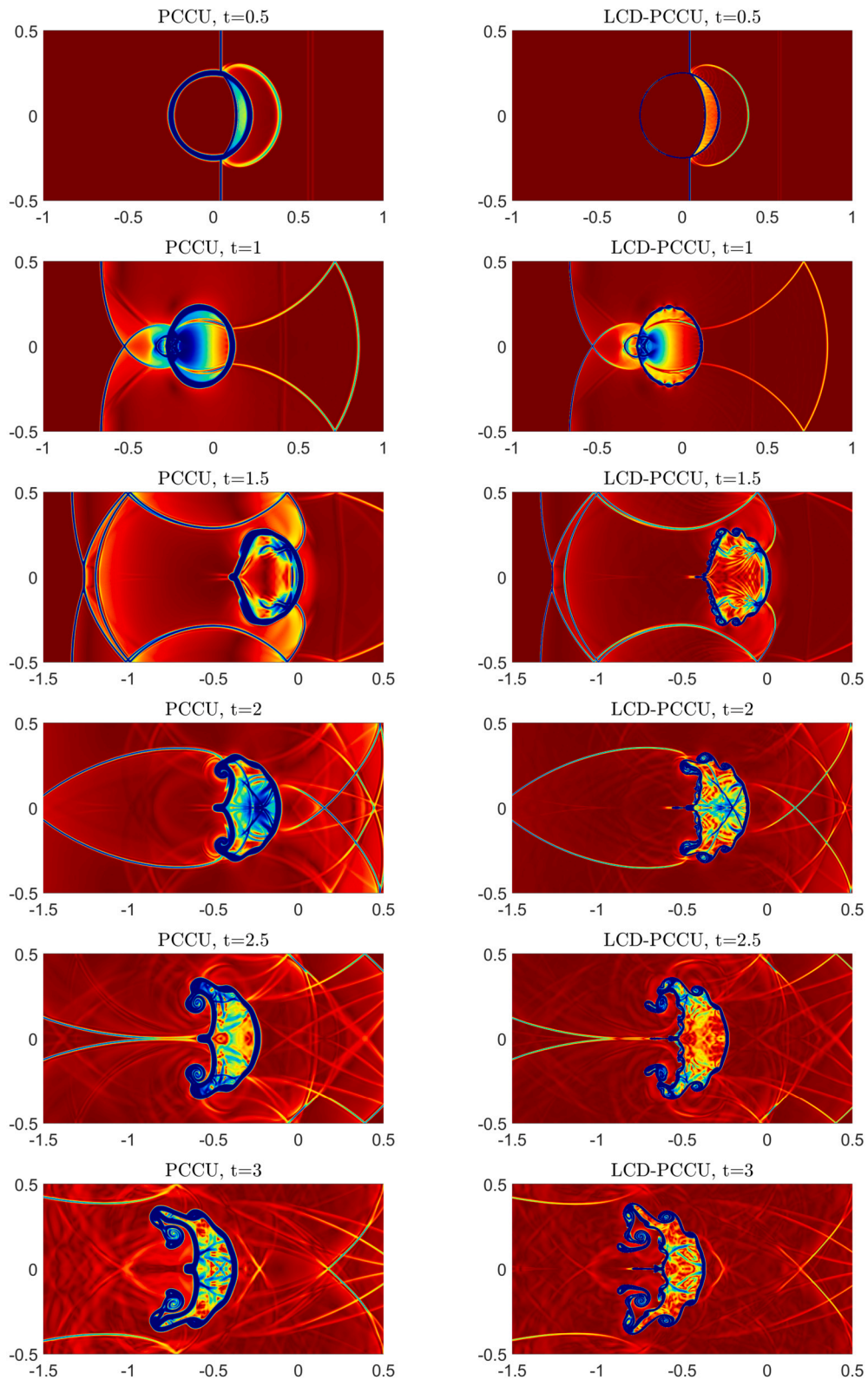


Fig. 5.5. Example 4: Shock-R22 bubble interaction by the PCCU (left column) and LCD-PCCU (right column) schemes at different times.

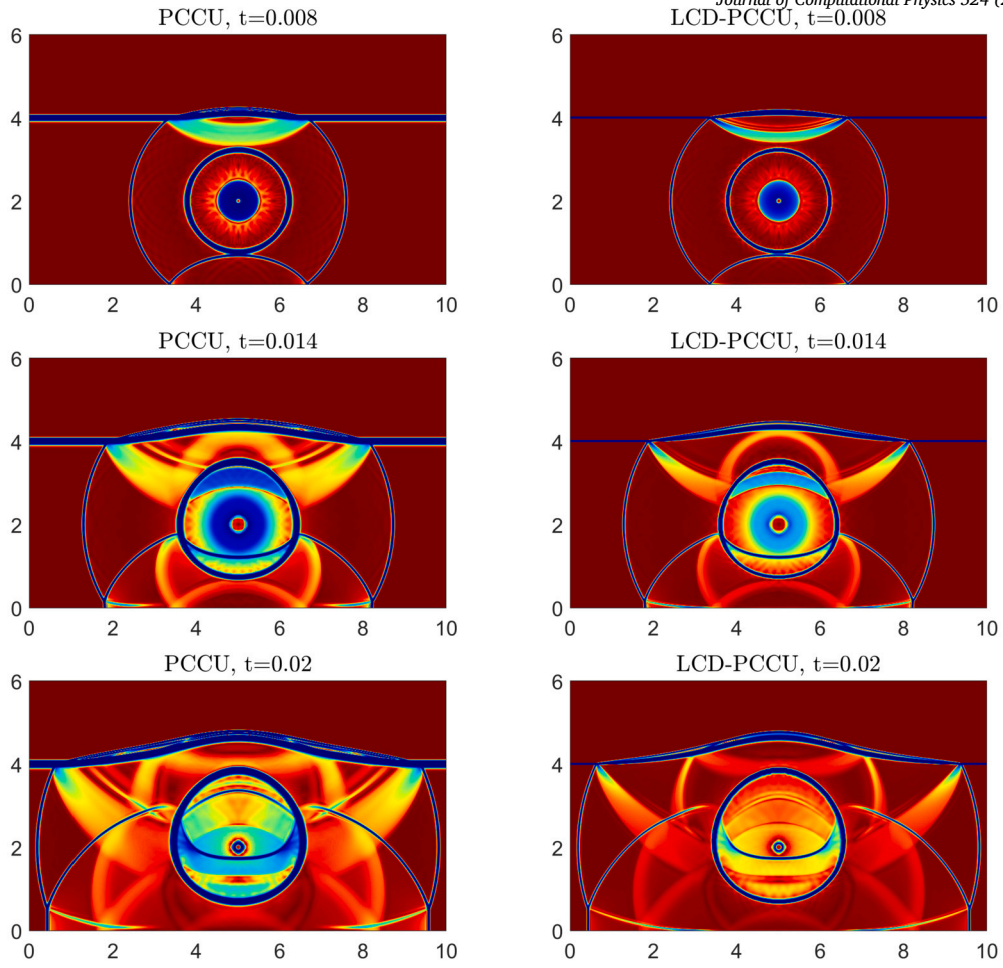


Fig. 5.6. Example 5: Time evolution of the solution computed by the PCCU (left column) and LCD-PCCU (right column) schemes.

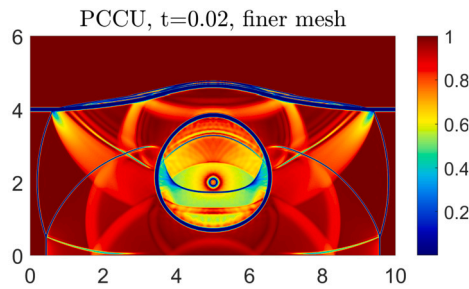


Fig. 5.7. Example 5: A finer mesh ( $\Delta x = \Delta y = 1/160$ ) PCCU solution at  $t = 0.02$ .

present the obtained result in Fig. 5.7, where one can clearly see that the PCCU solution computed on a finer mesh is close to the LCD-PCCU solution computed with  $\Delta x = \Delta y = 1/80$ . Once again, this indicates that the LCD-PCCU solution is more accurate than the PCCU one.

### 5.2. Thermal rotating shallow water equations

In this section, we apply the developed LCD-PCCU schemes to the 1-D and 2-D TRSW equations [27], which in the 2-D case can be written as the system (4.1) with

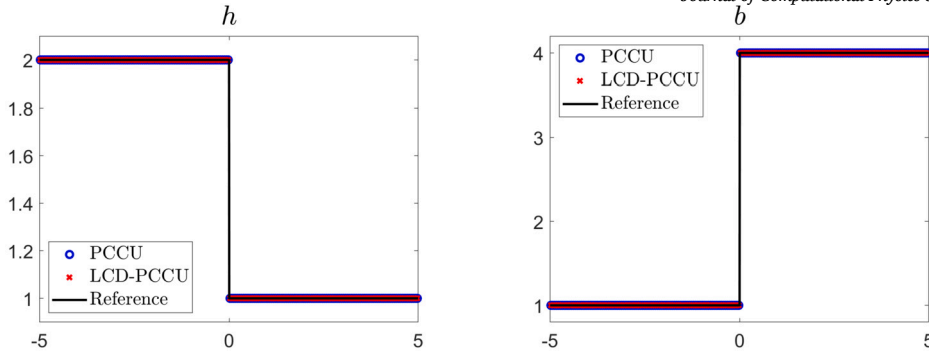


Fig. 5.8. Example 6:  $h$  and  $b$  computed by the PCCU and LCD-PCCU schemes.

$$\begin{aligned}
 \mathbf{U} &= (h, q, p, hb)^\top, \quad \mathbf{F}(\mathbf{U}) = \left( hu, hu^2 + \frac{b}{2}h^2, huv, hub \right)^\top, \\
 \mathbf{G}(\mathbf{U}) &= \left( hv, huv, hv^2 + \frac{b}{2}h^2, hvb \right)^\top, \quad \mathbf{B}(\mathbf{U}) = \mathbf{C}(\mathbf{U}) \equiv \mathbf{0}, \\
 \mathbf{S}^x(x, y, t, \mathbf{U}) &= (0, fhu - hbZ_x, 0, 0)^\top, \quad \mathbf{S}^y(x, y, t, \mathbf{U}) = (0, 0, -fhu - hbZ_y, 0)^\top,
 \end{aligned} \tag{5.3}$$

where  $h$  denotes the thickness of the fluid layer,  $u$  and  $v$  are the zonal and meridional velocities,  $q := hu$  and  $p := hv$  are the corresponding discharges,  $b$  is the layer-averaged buoyancy variable, and  $Z(x, y)$  stands for a time-independent bottom topography. In the oceanic context,  $b = g\rho/\rho_0$ , where  $g$  is the acceleration due to gravity,  $\rho$  and  $\rho_0$  are the variable and constant parts of the water density, respectively. In the atmospheric context, the densities  $\rho$  and  $\rho_0$  should be replaced with the potential temperatures  $\theta$  and  $\theta_0$ . Finally,  $f(y) = f_0 + \beta y$  is the Coriolis parameter, where  $f_0$  and  $\beta$  are positive constants.

**Remark 5.4.** For the TRSW equations, we use the equilibrium variables introduced in [2] and compute the point values ( $\mathbf{U}_{k+\frac{1}{2}}^\pm$  and  $\check{\mathbf{U}}_{k+\frac{1}{2}}^\pm$  in the 1-D case and  $\mathbf{U}_{j,k}^E, \mathbf{U}_{j+1,k}^W, \mathbf{U}_{j,k}^N, \mathbf{U}_{j,k+1}^S, \check{\mathbf{U}}_{j,k}^E, \check{\mathbf{U}}_{j+1,k}^W, \check{\mathbf{U}}_{j,k}^N$ , and  $\check{\mathbf{U}}_{j,k+1}^S$  in the 2-D case) as well as the global fluxes ( $\mathbf{L}_{k+\frac{1}{2}}^\pm$  in the 1-D case and  $\mathbf{K}(\mathbf{U}_{j,k}^W), \mathbf{K}(\mathbf{U}_{j+1,k}^W), \mathbf{L}(\mathbf{U}_{j,k}^N)$ , and  $\mathbf{L}(\mathbf{U}_{j,k+1}^S)$  in the 2-D case) precisely as it was done in [2]. We have also used the same numerical diffusion switch function, which helps to enforce the WB property, as in [2].

**Remark 5.5.** In Appendix B, we provide the expressions for the matrices  $\hat{\mathcal{A}}_{k+\frac{1}{2}}$  and  $\hat{\mathcal{A}}_{j+\frac{1}{2},k}^F$  and the corresponding matrices  $R_{k+\frac{1}{2}}$  and  $R_{j+\frac{1}{2},k}$  for the 1-D and 2-D TRSW equations, respectively. The matrices  $\hat{\mathcal{A}}_{j,k+\frac{1}{2}}^G$  and  $R_{j,k+\frac{1}{2}}$  can be obtained in an analogous way.

### 5.2.1. One-dimensional examples

In this section, we consider two numerical examples for the so-called 1-D Ripa system, which is the 1-D version of (4.1), (5.3), but with  $f(y) \equiv 0$ :

$$\begin{cases} h_t + (hv)_y = 0, \\ p_t + \left( hv^2 + \frac{b}{2}h^2 \right)_y = -hbZ_y, \\ (hb)_t + (hvb)_y = 0. \end{cases}$$

#### Example 6—constant pressure equilibrium

In the first example taken from [2], we consider the following initial data:

$$(h, v, b)(y, 0) = \begin{cases} (2, 0, 1) & \text{if } y < 0, \\ (1, 0, 4) & \text{otherwise,} \end{cases} \tag{5.4}$$

which are prescribed in the computational domain  $[-5, 5]$  together with the flat bottom topography  $Z(y) \equiv 0$  subject to the free boundary conditions.

We first compute the numerical solution by the PCCU and LCD-PCCU schemes until the final time  $t = 10$  on the uniform mesh with  $\Delta x = 1/20$  and plot the obtained fluid thickness  $h$  and buoyancy variables  $b$  in Fig. 5.8, where the reference solution is computed by the PCCU scheme on a much finer mesh with  $\Delta x = 1/400$ . We stress that both the PCCU and LCD-PCCU schemes can exactly preserve the steady state and the obtained errors for both  $h$  and  $b$  are zeros.

We then test the ability of the proposed schemes to capture small perturbations of this steady state. To this end, we first denote by  $h_{\text{eq}}(y) = h(y, 0)$  given by (5.4), and then modify the initial condition of  $h$  in the following manner:

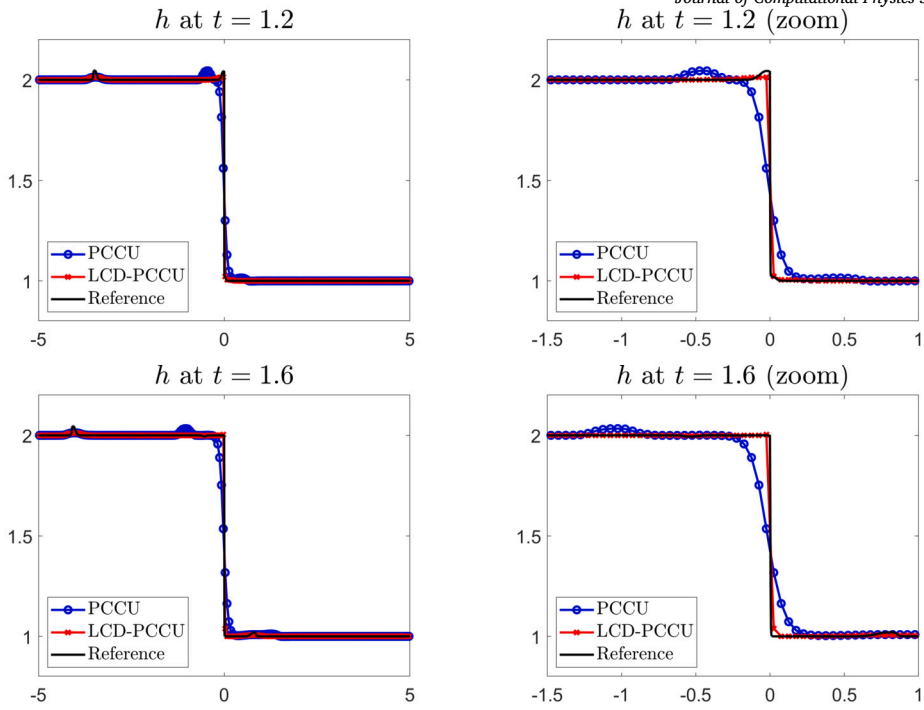


Fig. 5.9. Example 6:  $h$  computed by the PCCU and LCD-PCCU schemes at  $t = 1.2$  (top row) and  $1.6$  (bottom row) and zoom at  $x \in [-1.5, 1]$  (right column).

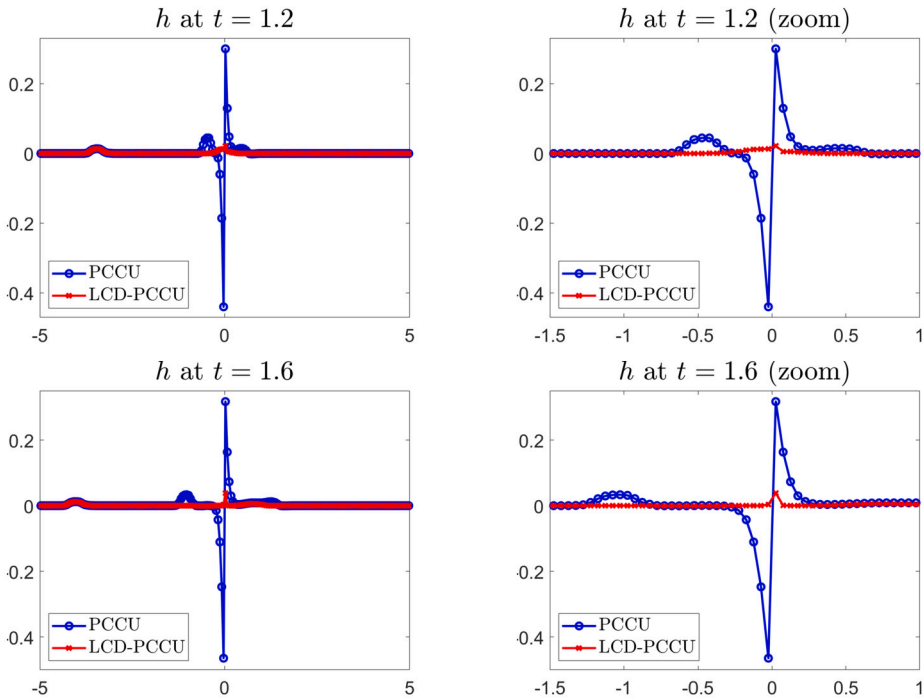


Fig. 5.10. Example 6:  $h - h_{eq}$  computed by the PCCU and LCD-PCCU schemes at  $t = 1.2$  (top row) and  $1.6$  (bottom row) and zoom at  $x \in [-1.5, 1]$  (right column).

$$h(y, 0) = h_{eq}(y) + \begin{cases} 0.1 & \text{if } y \in [-1.8, -1.7], \\ 0 & \text{otherwise.} \end{cases}$$

We compute the solution until the final time  $t = 1.6$  on a uniform mesh with  $\Delta x = 1/20$  and plot the obtained fluid thickness together with the reference solution computed by the LCD-PCCU scheme on a much finer mesh with  $\Delta x = 1/400$  (Fig. 5.9) and the difference between the perturbed and steady solutions (Fig. 5.10) at times  $t = 1.2$  and  $1.6$ . One can clearly see that the LCD-PCCU scheme

**Table 5.3**  
 Example 6:  $L^1$ -errors in  $h$  computed by the PCCU and LCD-PCCU schemes and the corresponding experimental convergence rates at  $t = 1.2$ .

	$\Delta x = 1/20$	$\Delta x = 1/40$	Rate	$\Delta x = 1/80$	Rate
PCCU	8.16e-2	4.72e-2	0.790	2.49e-2	0.923
LCD-PCCU	1.25e-2	8.55e-3	0.548	5.05e-3	0.760

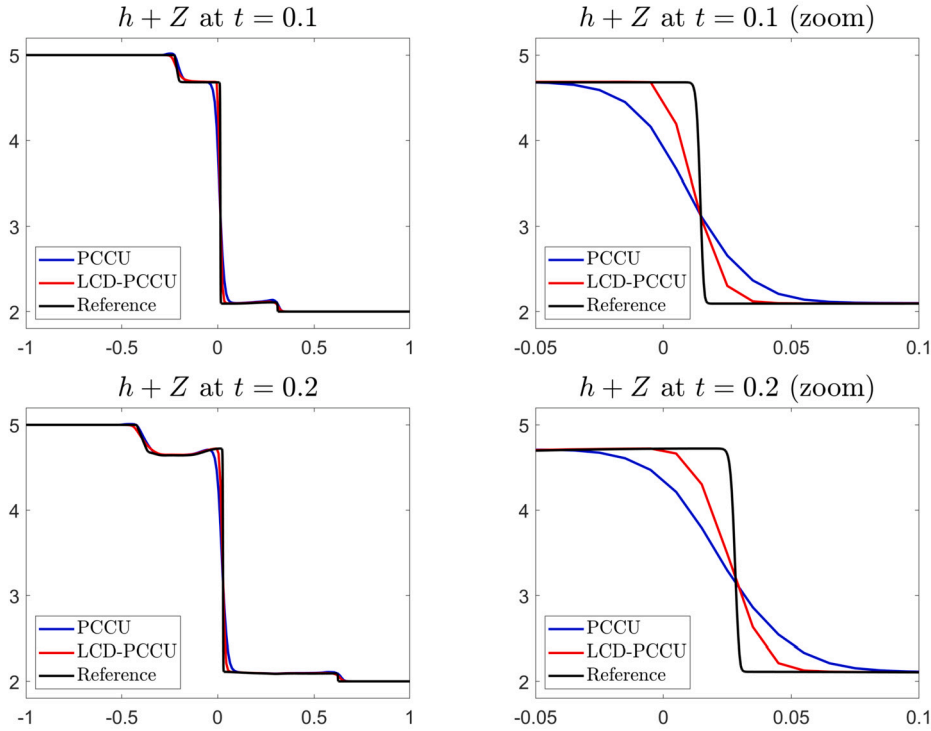


Fig. 5.11. Example 7:  $h + Z$  computed by the PCCU and LCD-PCCU schemes at  $t = 0.1$  (top row) and  $0.2$  (bottom row) and zoom at  $x \in [-0.05, 0.1]$  (right column).

achieves sharper resolution than the PCCU scheme. Moreover, the LCD-PCCU solution is substantially less oscillatory than the PCCU one. We also compute the  $L^1$ -errors (against the reference solution) in  $h$  computed by the PCCU and LCD-PCCU schemes at  $t = 1.2$ . The errors reported in Table 5.3, show that the LCD-PCCU scheme is much more accurate than its PCCU counterpart though the experimental convergence rates of the LCD-PCCU scheme is lower.

*Example 7—dam break over a nonflat bottom*

In the second example taken from [16], we consider the dam break problem subject to the following initial data:

$$(h, v, b)(y, 0) = \begin{cases} (5 - Z(y), 0, 1) & \text{if } y < 0, \\ (2 - Z(y), 0, 5) & \text{otherwise,} \end{cases}$$

and the nonflat bottom topography

$$Z(y) = \begin{cases} \cos(10\pi(x + 0.3)) + 1 & \text{if } -0.4 \leq y \leq -0.2, \\ \frac{1}{2} [\cos(10\pi(x - 0.3)) + 1] & 0.2 \leq y \leq 0.4, \\ 0 & \text{otherwise.} \end{cases}$$

The initial conditions are prescribed in the computational domain  $[-1, 1]$  subject to the free boundary conditions.

We compute the numerical solution by the PCCU and LCD-PCCU schemes until the final time  $t = 0.2$  on a uniform mesh with  $\Delta x = 1/100$  and plot the obtained water surface  $h + Z$  in Fig. 5.11, where the reference solution is computed by the PCCU scheme on a much finer mesh with  $\Delta x = 1/2000$ . One can clearly see that the LCD-PCCU scheme produces higher-resolution results than the PCCU one. We also compute the  $L^1$ -errors (against the reference solution) in  $h + Z$  computed by the PCCU and LCD-PCCU schemes at  $t = 0.2$ . The errors reported in Table 5.4, once again, show that the LCD-PCCU scheme is much more accurate than its PCCU counterpart.

**Table 5.4**

Example 7:  $L^1$ -errors in  $h + Z$  computed by the PCCU and LCD-PCCU schemes and the corresponding experimental convergence rates at  $t = 0.2$ .

	$\Delta x = 1/100$	$\Delta x = 1/200$	Rate	$\Delta x = 1/400$	Rate
PCCU	5.44e-2	3.08e-2	0.821	1.48e-2	1.057
LCD-PCCU	2.99e-2	1.65e-3	0.858	7.50e-3	1.137

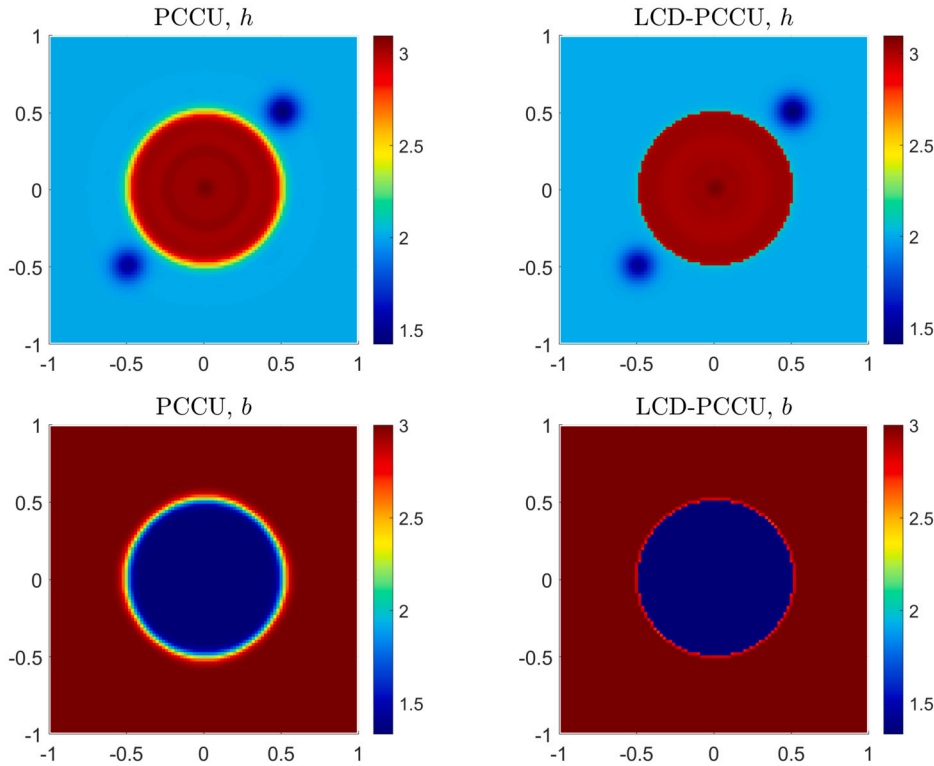


Fig. 5.12. Example 8:  $h$  and  $b$  computed by the PCCU (left column) and LCD-PCCU (right column) schemes.

5.2.2. Two-dimensional examples

In this section, we consider three numerical examples for the 2-D TRSW equations.

Example 8—small perturbations of a 2-D steady state

In this example taken from [16], we take  $f(y) \equiv 0$  and consider the following initial conditions:

$$(h, u, v, b)(x, y, 0) = \begin{cases} (3.1 - Z(x, y), 0, 0, \frac{4}{3}) & \text{if } 0.01 < x^2 + y^2 < 0.09, \\ (3 - Z(x, y), 0, 0, \frac{4}{3}) & \text{if } 0.09 < x^2 + y^2 < 0.25 \text{ or } x^2 + y^2 < 0.01, \\ (2 - Z(x, y), 0, 0, 3) & \text{otherwise,} \end{cases}$$

with the nonflat bottom topography consisting of two Gaussian shaped humps:

$$Z(x, y) = \begin{cases} 0.5 e^{-100[(x+0.5)^2 + (y+0.5)^2]} & \text{if } x < 0, \\ 0.6 e^{-100[(x-0.5)^2 + (y-0.5)^2]} & \text{otherwise.} \end{cases}$$

The initial data are prescribed in the computational domain  $[-1, 1] \times [-1, 1]$  subject to the free boundary conditions.

We compute the numerical solution by the PCCU and LCD-PCCU schemes until the final time  $t = 0.12$  on a uniform mesh with  $\Delta x = \Delta y = 1/50$ . The obtained results are presented in Fig. 5.12, where one can clearly see that the LCD-PCCU scheme outperforms the PCCU one, since the  $h$ - and  $b$ -components computed by the PCCU scheme are smeared; see Fig. 5.12. We also plot the 1-D slices of  $h$  and  $b$  along the diagonal  $y = x$ ; see Fig. 5.13, where the reference solution is computed by the PCCU scheme on a much finer mesh with  $\Delta x = \Delta y = 1/400$ . As one can see, the LCD-PCCU scheme achieves higher resolution than the PCCU one.

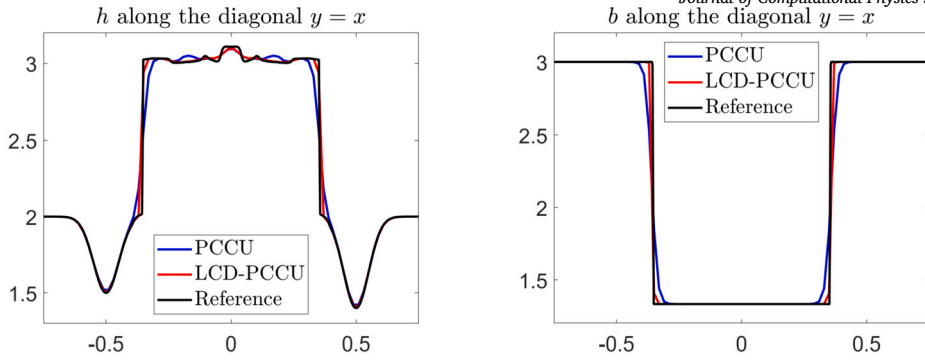


Fig. 5.13. Example 8: Diagonal slices of  $h$  (left) and  $b$  (right) computed by the PCCU and LCD-PCCU schemes; zoom at  $[-0.75, 0.75]$ .

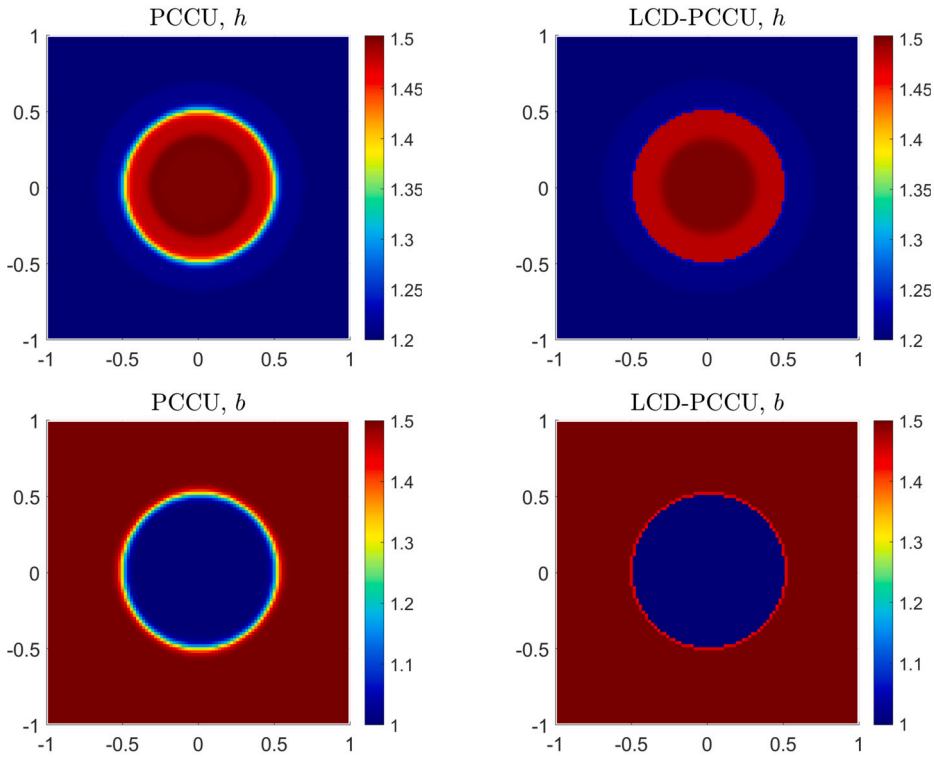


Fig. 5.14. Example 9:  $h$  and  $b$  computed by the PCCU (left column) and LCD-PCCU (right column) schemes.

*Example 9—radial dam break over the flat bottom*

In this example taken from [16], we compare the PCCU and LCD-PCCU schemes on a circular dam-break problem with a flat bottom topography ( $Z(x, y) \equiv 0$ ) and no Coriolis forces ( $f(y) \equiv 0$ ). The initial conditions,

$$(h, u, v, b)(x, y, 0) = \begin{cases} (1.5, 0, 0, 1) & \text{if } x^2 + y^2 < 0.25, \\ (1.2, 0, 0, 1.5) & \text{otherwise,} \end{cases}$$

are prescribed in the computational domain  $[-1, 1] \times [-1, 1]$  subject to the free boundary conditions.

We compute the numerical solution by the PCCU and LCD-PCCU schemes until the final time  $t = 0.15$  on a uniform mesh with  $\Delta x = \Delta y = 1/50$ . The computed results are presented in Fig. 5.14, where one can clearly see that the LCD-PCCU scheme outperforms the PCCU scheme. We also plot the 1-D slices of  $h$  and  $b$  along the diagonal  $y = x$ ; see Fig. 5.15, where the reference solution is computed by the PCCU scheme on a much finer mesh with  $\Delta x = \Delta y = 1/400$ . As one can see, the LCD-PCCU scheme outperforms its PCCU counterpart.

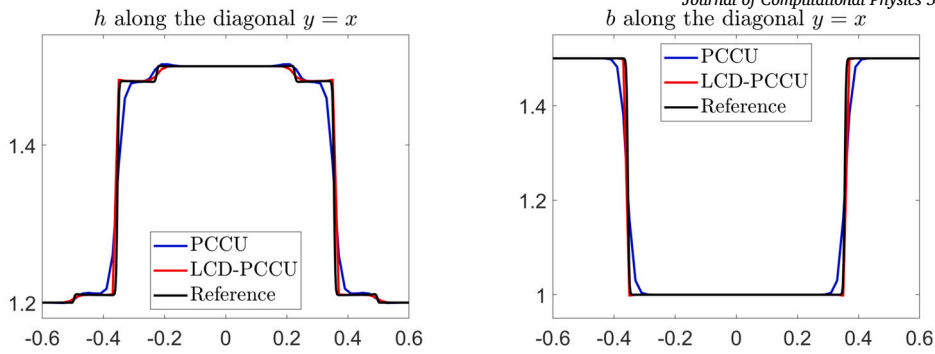


Fig. 5.15. Example 9: Diagonal slices of  $h$  (left) and  $b$  (right) computed by the PCCU and LCD-PCCU schemes; zoom at  $[-0.6, 0.6]$ .

#### Example 10—relaxation of localized anomalies on the equatorial $\beta$ -plane

In the last example taken from [27], we consider the relaxation of localized anomalies on the  $\beta$ -plane, where the Coriolis parameter is  $f(y) = y$ , with the initial data

$$h(x, y, 0) \equiv 1, \quad q(x, y, 0) = p(x, y, 0) \equiv 0, \quad b(x, y, 0) = 1 + \frac{1}{2} e^{-\left(\frac{1}{50}x^2 + \frac{1}{2}y^2\right)},$$

prescribed in the computational domain  $[-40, 80] \times [-10, 10]$  subject to the free boundary conditions.

We compute the numerical solution by the PCCU and LCD-PCCU schemes until the final time  $t = 120$  on a uniform mesh with  $\Delta x = \Delta y = 2/15$  and plot the obtained numerical results in Fig. 5.16, where one can see that our results are consistent with those reported in [27], and at the same time, the LCD-PCCU scheme outperforms the PCCU one. In order to better see the difference between the computed solutions, we also plot the 1-D slices of  $h$  along  $y = 0$  in Fig. 5.17, where the reference solution is computed by the PCCU scheme on a finer mesh with  $\Delta x = \Delta y = 1/25$ . One can see that the LCD-PCCU scheme achieves significantly better resolution than the PCCU one.

In this example, we also check the efficiency of the proposed LCD-PCCU scheme by performing a more thorough comparison between the studied schemes. To this end, we measure the CPU time consumed during the above calculations by the LCD-PCCU scheme and refine the mesh used by the PCCU scheme to the level that exactly the same CPU time is consumed to compute both of the numerical solutions: This way, we take into account additional computational cost of the LCD-PCCU scheme. The corresponding grids are  $\Delta x = \Delta y = 2/15$  for the LCD-PCCU scheme, and  $\Delta x = \Delta y = 1/9$  for the PCCU scheme. The obtained numerical results are plotted in Fig. 5.18, where one can clearly see that the LCD-PCCU solution is still more accurate than the PCCU one.

#### CRedit authorship contribution statement

**Shaoshuai Chu:** Writing – review & editing, Writing – original draft, Visualization, Validation, Software, Methodology, Investigation, Formal analysis, Conceptualization. **Michael Herty:** Writing – review & editing, Methodology, Investigation, Funding acquisition, Conceptualization. **Alexander Kurganov:** Writing – review & editing, Writing – original draft, Visualization, Validation, Supervision, Project administration, Methodology, Investigation, Funding acquisition, Formal analysis, Conceptualization.

#### Declaration of competing interest

The authors declare that they have no known competing financial interests or personal relationships that could have appeared to influence the work reported in this paper.

#### Acknowledgements

The work of S. Chu was supported in part by the DFG (German Research Foundation) through HE5386/19-3, 27-1. The work of M. Herty was funded by the DFG–SPP 2183: Eigenschaftsgeregelte Umformprozesse with the Project(s) HE5386/19-2,19-3 Entwicklung eines flexiblen isothermen Reckschmiedeprozesses für die eigenschaftsgeregelte Herstellung von Turbinenschaufeln aus Hochtemperaturwerkstoffen (424334423) and by the Deutsche Forschungsgemeinschaft (DFG, German Research Foundation)–SPP 2410 Hyperbolic Balance Laws in Fluid Mechanics: Complexity, Scales, Randomness (CoScaRa) within the Project(s) HE5386/26-1 (Numerische Verfahren für gekoppelte Mehrskalprobleme, 525842915) and (Zufällige kompressible Euler Gleichungen: Numerik und ihre Analysis, 525853336) HE5386/27-1. The work of A. Kurganov was supported in part by NSFC grant 12171226 and by the fund of the Guangdong Provincial Key Laboratory Of Computational Science And Material Design (No. 2019B030301001).

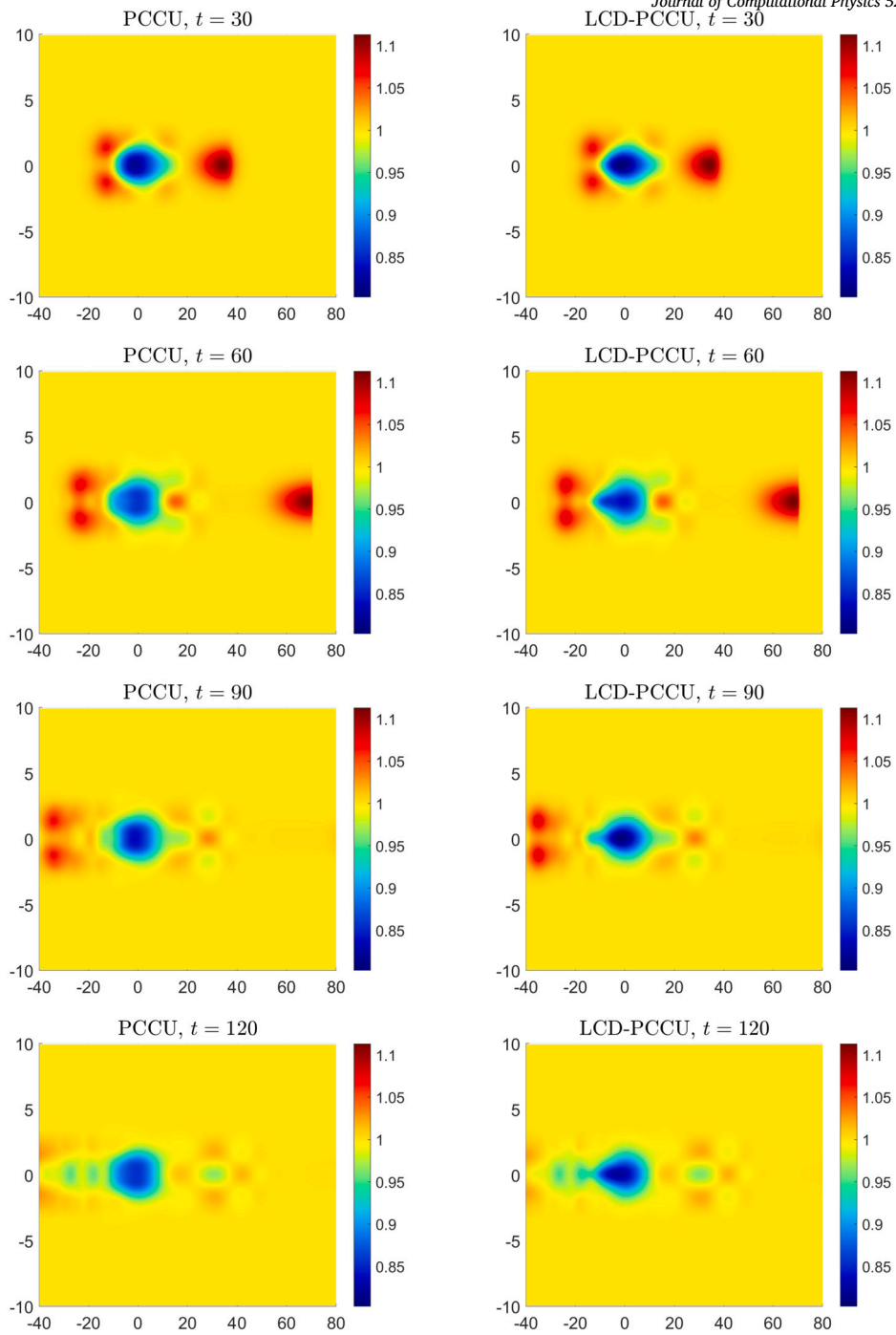


Fig. 5.16. Example 10: Time snapshots of  $h$  computed by the PCCU (left column) and LCD-PCCU (right column) schemes.

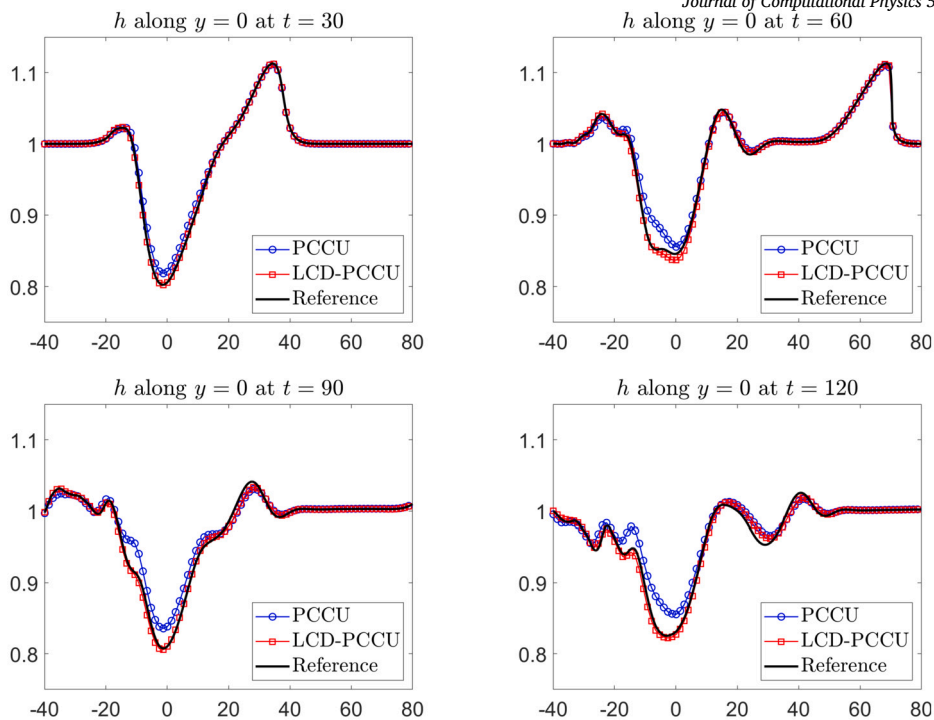


Fig. 5.17. Example 10: Slices of  $h$  and  $b$  along the line  $y=0$  computed by the PCCU and LCD-PCCU schemes using  $\Delta x = \Delta y = 2/15$  at different times.

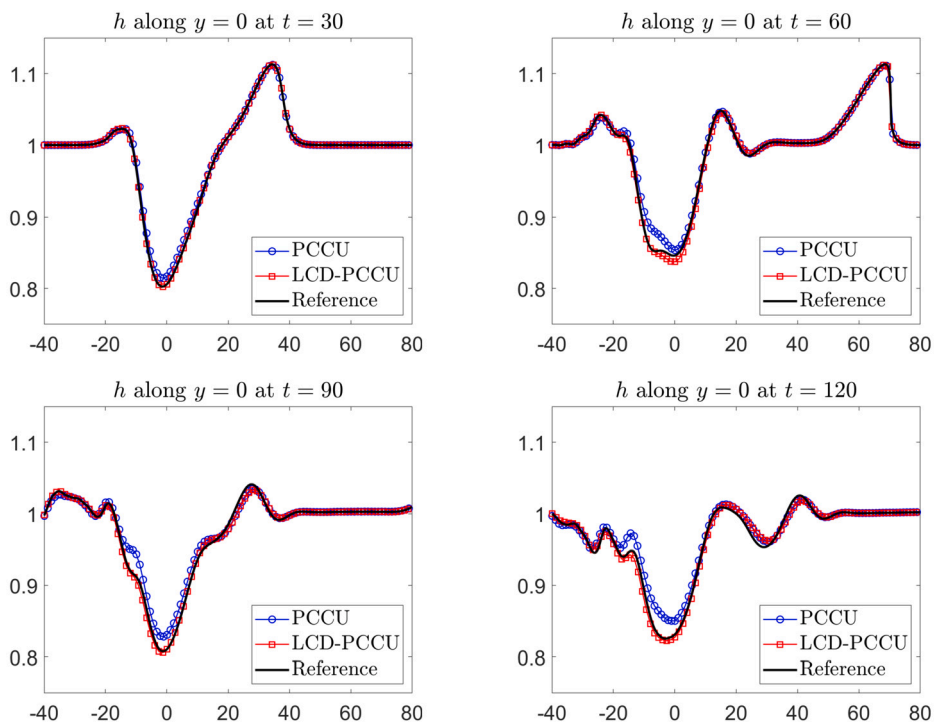


Fig. 5.18. Example 10: Slices of  $h$  and  $b$  along the line  $y=0$  computed by the PCCU scheme using  $\Delta x = \Delta y = 1/9$  and LCD-PCCU scheme using  $\Delta x = \Delta y = 2/15$  at different times.

**Appendix A. LCD matrices for the  $\gamma$ -based compressible multifluid equations**

*A.1. One-dimensional case*

In order to compute the LCD matrices for the 1-D  $\gamma$ -based compressible multifluid system, we first compute the matrix  $\mathcal{A} = \frac{\partial F}{\partial U} - B$ :

$$\mathcal{A}(U) = \begin{pmatrix} 0 & 1 & 0 & 0 & 0 \\ \frac{\gamma-3}{2}u^2 & (3-\gamma)u & \gamma-1 & (1-\gamma)p & 1-\gamma \\ \frac{uc^2}{1-\gamma} + \left(\frac{\gamma}{2}-1\right)u^3 & \frac{c^2}{\gamma-1} + \left(\frac{3}{2}-\gamma\right)u^2 & \gamma u & (1-\gamma)pu & (1-\gamma)u \\ 0 & 0 & 0 & u & 0 \\ 0 & 0 & 0 & 0 & u \end{pmatrix}, \tag{A.1}$$

where  $c = \sqrt{\frac{\gamma(p+\pi_\infty)}{\rho}}$  is the speed of sound, and then introduce  $\hat{\mathcal{A}}_{j+\frac{1}{2}} = \mathcal{A}(\hat{U}_{j+\frac{1}{2}})$ , which is given by (A.1) with  $\gamma, u, p$ , and  $c$  replaced with

$$\hat{\gamma} = \frac{\gamma_j + \gamma_{j+1}}{2}, \quad \hat{u} = \frac{u_j + u_{j+1}}{2}, \quad \hat{p} = \frac{p_j + p_{j+1}}{2}, \quad \text{and} \quad \hat{c} = \sqrt{\frac{\hat{\gamma}(\hat{p} + \hat{\pi}_\infty)}{\hat{\rho}}},$$

respectively. Here,

$$\begin{aligned} \gamma_j &= \frac{1}{\bar{\Gamma}_j} + 1, \quad (\pi_\infty)_j = \frac{\bar{\Pi}_j}{\bar{\Gamma}_j + 1}, \quad \hat{\rho} = \frac{\bar{\rho}_j + \bar{\rho}_{j+1}}{2}, \quad u_j = \frac{(\bar{\rho}u)_j}{\bar{\rho}_j}, \\ p_j &= (\gamma_j - 1) \left[ \bar{E}_j - \frac{1}{2} \bar{\rho}_j u_j^2 \right] - \gamma_j (\pi_\infty)_j, \quad \hat{\pi}_\infty = \frac{(\pi_\infty)_j + (\pi_\infty)_{j+1}}{2}. \end{aligned}$$

Notice that all of the  $(\hat{\cdot})$  quantities have to have a subscript index, that is,  $(\hat{\cdot}) = (\hat{\cdot})_{j+\frac{1}{2}}$ , but we omit it for the sake of brevity for all of the quantities except for  $\hat{\mathcal{A}}_{j+\frac{1}{2}}$ . We then compute the matrix  $R_{j+\frac{1}{2}}$  composed of the right eigenvectors of  $\hat{\mathcal{A}}_{j+\frac{1}{2}}$  and obtain

$$\begin{aligned} R_{j+\frac{1}{2}} &= \begin{pmatrix} 1 & 1 & 0 & 0 & 1 \\ \hat{u} - \hat{c} & \hat{u} & 0 & 0 & \hat{u} + \hat{c} \\ \frac{\hat{c}^2}{\hat{\gamma} - 1} + \frac{1}{2}\hat{u}^2 - \hat{u}\hat{c} & \frac{\hat{u}^2}{2} & \hat{p} & 0 & \frac{\hat{c}^2}{\hat{\gamma} - 1} + \frac{1}{2}\hat{u}^2 + \hat{u}\hat{c} \\ 0 & 0 & 1 & -1 & 0 \\ 0 & 0 & 0 & \hat{p} & 0 \end{pmatrix}, \\ R_{j+\frac{1}{2}}^{-1} &= \frac{1}{2\hat{c}^2} \begin{pmatrix} \frac{(\hat{\gamma} - 1)\hat{u}^2}{2} + \hat{u}\hat{c} & -\hat{c} - (\hat{\gamma} - 1)\hat{u} & \hat{\gamma} - 1 & (1 - \hat{\gamma})\hat{p} & 1 - \hat{\gamma} \\ 2\hat{c}^2 - (\hat{\gamma} - 1)\hat{u}^2 & 2(\hat{\gamma} - 1)\hat{u} & 2(1 - \hat{\gamma}) & 2(\hat{\gamma} - 1)\hat{p} & 2(\hat{\gamma} - 1) \\ 0 & 0 & 0 & 2\hat{c}^2 & \frac{2\hat{c}^2}{\hat{p}} \\ 0 & 0 & 0 & 0 & -\frac{2\hat{c}^2}{\hat{p}} \\ \frac{(\hat{\gamma} - 1)\hat{u}^2}{2} - \hat{u}\hat{c} & \hat{c} - (\hat{\gamma} - 1)\hat{u} & \hat{\gamma} - 1 & (1 - \hat{\gamma})\hat{p} & 1 - \hat{\gamma} \end{pmatrix}. \end{aligned}$$

*A.2. Two-dimensional case*

We now compute the matrix  $\hat{\mathcal{A}}_{j+\frac{1}{2},k}^F$  and the corresponding matrices  $R_{j+\frac{1}{2},k}$  and  $R_{j+\frac{1}{2},k}^{-1}$  for the 2-D  $\gamma$ -based compressible multifluid system.

We first compute  $\mathcal{A}^F = \frac{\partial F}{\partial U} - B$ :

$$\mathcal{A}^F(U) = \begin{pmatrix} 0 & 1 & 0 & 0 & 0 & 0 \\ \frac{\gamma-3}{2}u^2 + \frac{\gamma-1}{2}v^2 & (3-\gamma)u & (1-\gamma)v & \gamma-1 & (1-\gamma)p & 1-\gamma \\ -uv & v & u & 0 & 0 & 0 \\ \frac{uc^2}{1-\gamma} + \left(\frac{\gamma}{2}-1\right)u(u^2+v^2) & \frac{c^2}{\gamma-1} + \left(\frac{3}{2}-\gamma\right)u^2 + \frac{1}{2}v^2 & (1-\gamma)uv & \gamma u & (1-\gamma)pu & (1-\gamma)u \\ 0 & 0 & 0 & 0 & u & 0 \\ 0 & 0 & 0 & 0 & 0 & u \end{pmatrix}, \tag{A.2}$$

and then introduce the matrix  $\hat{\mathcal{A}}_{j+\frac{1}{2},k}^F = \mathcal{A}(\hat{U}_{j+\frac{1}{2},k})$ , which is given by (A.2) with  $\gamma$ ,  $u$ ,  $v$ ,  $p$ , and  $c$  replaced with

$$\hat{\gamma} = \frac{\gamma_{j,k} + \gamma_{j+1,k}}{2}, \quad \hat{u} = \frac{u_{j,k} + u_{j+1,k}}{2}, \quad \hat{v} = \frac{v_{j,k} + v_{j+1,k}}{2}, \quad \hat{p} = \frac{p_{j,k} + p_{j+1,k}}{2}, \quad \hat{c} = \sqrt{\frac{\hat{\gamma}(\hat{p} + \hat{\pi}_\infty)}{\hat{p}}},$$

respectively. Here,

$$\gamma_{j,k} = \frac{1}{\bar{\Gamma}_{j,k}} + 1, \quad (\pi_\infty)_{j,k} = \frac{\bar{\Pi}_{j,k}}{\bar{\Gamma}_{j,k} + 1}, \quad \hat{p} = \frac{\bar{\rho}_{j,k} + \bar{\rho}_{j+1,k}}{2}, \quad u_{j,k} = \frac{(\bar{\rho}u)_{j,k}}{\bar{\rho}_{j,k}}, \quad v_{j,k} = \frac{(\bar{\rho}v)_{j,k}}{\bar{\rho}_{j,k}},$$

$$p_{j,k} = (\gamma_{j,k} - 1) \left[ \bar{E}_{j,k} - \frac{1}{2} \bar{\rho}_{j,k} u_{j,k}^2 - \frac{1}{2} \bar{\rho}_{j,k} v_{j,k}^2 \right] - \gamma_{j,k} (\pi_\infty)_{j,k}, \quad \hat{\pi}_\infty = \frac{(\pi_\infty)_{j,k} + (\pi_\infty)_{j+1,k}}{2}.$$

Notice that all of the  $(\hat{\cdot})$  quantities have to have a subscript index, that is,  $(\hat{\cdot}) = (\hat{\cdot})_{j+\frac{1}{2},k}$ , but we omit it for the sake of brevity for all of the quantities except for  $\hat{\mathcal{A}}_{j+\frac{1}{2},k}^F$ . We then compute the matrix  $R_{j+\frac{1}{2},k}$  composed of the right eigenvectors of  $\hat{\mathcal{A}}_{j+\frac{1}{2},k}^F$  and obtain

$$R_{j+\frac{1}{2},k} = \begin{pmatrix} 1 & 1 & 0 & 0 & 0 & 1 \\ \hat{u} - \hat{c} & \hat{u} & 0 & 0 & 0 & \hat{u} + \hat{c} \\ \hat{v} & \hat{v} & 1 & 0 & 0 & \hat{v} \\ \frac{\hat{c}^2}{\hat{\gamma} - 1} + \frac{1}{2} \hat{u}^2 + \frac{1}{2} \hat{v}^2 - \hat{u}\hat{c} & \frac{\hat{u}^2 + \hat{v}^2}{2} & \hat{v} & \hat{p} & 0 & \frac{\hat{c}^2}{\hat{\gamma} - 1} + \frac{1}{2} \hat{u}^2 + \frac{1}{2} \hat{v}^2 + \hat{u}\hat{c} \\ 0 & 0 & 0 & 1 & 1 & 0 \\ 0 & 0 & 0 & 0 & -\hat{p} & 0 \end{pmatrix}$$

$$R_{j+\frac{1}{2},k}^{-1} = \frac{1}{2\hat{c}^2} \begin{pmatrix} \frac{(\hat{\gamma} - 1)(\hat{u}^2 + \hat{v}^2)}{2} + \hat{u}\hat{c} & -\hat{c} - (\hat{\gamma} - 1)\hat{u} & (1 - \hat{\gamma})\hat{v} & \hat{\gamma} - 1 & (1 - \hat{\gamma})\hat{p} & 1 - \hat{\gamma} \\ 2\hat{c}^2 - (\hat{\gamma} - 1)(\hat{u}^2 + \hat{v}^2) & 2(\hat{\gamma} - 1)\hat{u} & 2(\hat{\gamma} - 1)\hat{v} & 2(1 - \hat{\gamma}) & 2(\hat{\gamma} - 1)\hat{p} & 2(\hat{\gamma} - 1) \\ -2\hat{c}^2\hat{v} & 0 & 2\hat{c}^2 & 0 & 0 & 0 \\ 0 & 0 & 0 & 0 & 2\hat{c}^2 & \frac{2\hat{c}^2}{\hat{p}} \\ \frac{(\hat{\gamma} - 1)(\hat{u}^2 + \hat{v}^2)}{2} - \hat{u}\hat{c} & \hat{c} - (\hat{\gamma} - 1)\hat{u} & (1 - \hat{\gamma})\hat{v} & \hat{\gamma} - 1 & (1 - \hat{\gamma})\hat{p} & 1 - \hat{\gamma} \end{pmatrix}.$$

## Appendix B. LCD matrices for the TRSW equations

### B.1. One-dimensional case

In order to compute the LCD matrices for the 1-D TRSW equations, we first compute the matrix  $\mathcal{A} = \frac{\partial G}{\partial U} - C$ :

$$\mathcal{A}(U) = \begin{pmatrix} 0 & 0 & 1 & 0 \\ -uv & v & u & 0 \\ \frac{bh}{2} - v^2 & 0 & 2v & \frac{h}{2} \\ -bv & 0 & b & v \end{pmatrix}, \quad (\text{B.1})$$

and then introduce the matrices  $\hat{\mathcal{A}}_{k+\frac{1}{2}} = \mathcal{A}(\hat{U}_{k+\frac{1}{2}})$ , which are given by (B.1) with  $h$ ,  $u$ ,  $v$ , and  $b$  replaced with

$$\hat{h} = \frac{\bar{h}_k + \bar{h}_{k+1}}{2}, \quad \hat{u} = \frac{u_k + u_{k+1}}{2}, \quad \hat{v} = \frac{v_k + v_{k+1}}{2}, \quad \hat{b} = \frac{b_k + b_{k+1}}{2},$$

respectively. Here,  $u_k = \bar{q}_k / \bar{h}_k$ ,  $v_k = \bar{p}_k / \bar{h}_k$ , and  $b_k = \overline{(hb)}_k / \bar{h}_k$ .

Notice that all of the  $(\hat{\cdot})$  quantities have to have a subscript index, that is,  $(\hat{\cdot}) = (\hat{\cdot})_{k+\frac{1}{2}}$ , but we omit it for the sake of brevity for all of the quantities except for  $\hat{\mathcal{A}}_{k+\frac{1}{2}}$ . We then compute the matrix  $R_{k+\frac{1}{2}}$  composed of the right eigenvectors of  $\hat{\mathcal{A}}_{k+\frac{1}{2}}$  and obtain

$$R_{k+\frac{1}{2}} = \frac{1}{\hat{b}} \begin{pmatrix} 1 & -1 & 0 & 1 \\ \hat{u} & 0 & \hat{b} & \hat{u} \\ \hat{v} - \sqrt{\hat{b}\hat{h}} & -\hat{v} & 0 & \hat{v} + \sqrt{\hat{b}\hat{h}} \\ \hat{b} & \hat{b} & 0 & \hat{b} \end{pmatrix}, \quad R_{k+\frac{1}{2}}^{-1} = \frac{1}{4} \begin{pmatrix} \hat{b} + 2\hat{v}\sqrt{\frac{\hat{b}}{\hat{h}}} & 0 & -2\sqrt{\frac{\hat{b}}{\hat{h}}} & 1 \\ -2\hat{b} & 0 & 0 & 2 \\ -2\hat{u} & 4 & 0 & -2\frac{\hat{u}}{\hat{b}} \\ \hat{b} - 2\hat{v}\sqrt{\frac{\hat{b}}{\hat{h}}} & 0 & 2\sqrt{\frac{\hat{b}}{\hat{h}}} & 1 \end{pmatrix}.$$

B.2. Two-dimensional case

We now compute the matrix  $\hat{\mathcal{A}}_{j+\frac{1}{2},k}^F$  and the corresponding matrices  $R_{j+\frac{1}{2},k}$  and  $R_{j+\frac{1}{2},k}^{-1}$  for the 2-D TRSW equations.

We first compute  $\mathcal{A}^F = \frac{\partial F}{\partial U} - B$ :

$$\mathcal{A}^F(\mathbf{U}) = \begin{pmatrix} 0 & 1 & 0 & 0 \\ \frac{bh}{2} - u^2 & 2u & 0 & \frac{h}{2} \\ -uv & v & u & 0 \\ -bu & b & 0 & u \end{pmatrix}, \tag{B.2}$$

and then introduce the matrices  $\hat{\mathcal{A}}_{j+\frac{1}{2},k}^F = \mathcal{A}(\hat{\mathbf{U}}_{j+\frac{1}{2},k})$ , which are given by (B.2) with  $h, u, v$ , and  $b$  replaced with

$$\hat{h} = \frac{\bar{h}_{j,k} + \bar{h}_{j+1,k}}{2}, \quad \hat{u} = \frac{u_{j,k} + u_{j+1,k}}{2}, \quad \hat{v} = \frac{v_{j,k} + v_{j+1,k}}{2}, \quad \hat{b} = \frac{b_{j,k} + b_{j+1,k}}{2},$$

respectively. Here  $u_k = \bar{q}_{j,k}/\bar{h}_{j,k}$ ,  $v_k = \bar{p}_{j,k}/\bar{h}_{j,k}$ , and  $b_k = \overline{(hb)}_{j,k}/\bar{h}_{j,k}$ .

Notice that all of the  $(\hat{\cdot})$  quantities have to have a subscript index, that is,  $(\hat{\cdot}) = (\hat{\cdot})_{j+\frac{1}{2},k}$ , but we omit it for the sake of brevity for all of the quantities except for  $\hat{\mathcal{A}}_{j+\frac{1}{2},k}^F$ . We then compute the matrix  $R_{j+\frac{1}{2},k}$  composed of the right eigenvectors of  $\hat{\mathcal{A}}_{j+\frac{1}{2},k}^F$  and obtain

$$R_{j+\frac{1}{2},k} = \frac{1}{\hat{b}} \begin{pmatrix} 1 & -1 & 0 & 1 \\ \hat{u} - \sqrt{\hat{b}\hat{h}} & -\hat{u} & 0 & \hat{u} + \sqrt{\hat{b}\hat{h}} \\ \hat{v} & 0 & \hat{b} & \hat{v} \\ \hat{b} & \hat{b} & 0 & \hat{b} \end{pmatrix}, \quad R_{j+\frac{1}{2},k}^{-1} = \frac{1}{4} \begin{pmatrix} \hat{b} + 2\hat{u}\sqrt{\frac{\hat{b}}{\hat{h}}} & 0 & -2\sqrt{\frac{\hat{b}}{\hat{h}}} & 1 \\ -2\hat{b} & 0 & 0 & 2 \\ -2\hat{v} & 0 & 4 & -2\frac{\hat{v}}{\hat{b}} \\ \hat{b} - 2\hat{u}\sqrt{\frac{\hat{b}}{\hat{h}}} & 2\sqrt{\frac{\hat{b}}{\hat{h}}} & 0 & 1 \end{pmatrix}.$$

Data availability

Data will be made available on request.

References

- [1] S. Busto, M. Dumbser, S. Gavrilyuk, K. Ivanova, On thermodynamically compatible finite volume methods and path-conservative ADER discontinuous Galerkin schemes for turbulent shallow water flows, *J. Sci. Comput.* 88 (2021) 28, 45 pp.
- [2] Y. Cao, A. Kurganov, Y. Liu, Flux globalization based well-balanced path-conservative central-upwind scheme for the thermal rotating shallow water equations, *Commun. Comput. Phys.* 34 (2023) 993–1042.
- [3] Y. Cao, A. Kurganov, Y. Liu, R. Xin, Flux globalization based well-balanced path-conservative central-upwind schemes for shallow water models, *J. Sci. Comput.* 92 (2022) 69, 31 pp.
- [4] Y. Cao, A. Kurganov, Y. Liu, V. Zeitlin, Flux globalization based well-balanced path-conservative central-upwind scheme for two-layer thermal rotating shallow water equations, *J. Comput. Phys.* 474 (2023) 111790, 29 pp.
- [5] V. Caselles, R. Donat, G. Haro, Flux-gradient and source-term balancing for certain high resolution shock-capturing schemes, *Comput. Fluids* 38 (2009) 16–36.
- [6] M.J. Castro, T. Morales de Luna, C. Parés, Well-balanced schemes and path-conservative numerical methods, in: *Handbook of Numerical Methods for Hyperbolic Problems*, in: *Handb. Numer. Anal.*, vol. 18, Elsevier/North-Holland, Amsterdam, 2017, pp. 131–175.
- [7] M.J. Castro, C. Parés, Well-balanced high-order finite volume methods for systems of balance laws, *J. Sci. Comput.* 82 (2020) 48, 48 pp.
- [8] M.J. Castro Díaz, A. Kurganov, T. Morales de Luna, Path-conservative central-upwind schemes for nonconservative hyperbolic systems, *ESAIM: Math. Model. Numer. Anal.* 53 (2019) 959–985.
- [9] C. Chalons, Path-conservative in-cell discontinuous reconstruction schemes for non conservative hyperbolic systems, *Commun. Math. Sci.* 18 (2020) 1–30.
- [10] Y. Chen, A. Kurganov, M. Na, A flux globalization based well-balanced path-conservative central-upwind scheme for the shallow water flows in channels, *ESAIM: Math. Model. Numer. Anal.* 57 (2023) 1087–1110.
- [11] J. Cheng, F. Zhang, T.G. Liu, A discontinuous Galerkin method for the simulation of compressible gas-gas and gas-water two-medium flows, *J. Comput. Phys.* 403 (2020) 109059, 29 pp.
- [12] A. Chertock, S. Chu, M. Herty, A. Kurganov, M. Lukáčová-Medviďová, Local characteristic decomposition based central-upwind scheme, *J. Comput. Phys.* 473 (2023) 111718, 24 pp.
- [13] A. Chertock, S. Chu, A. Kurganov, Hybrid multifluid algorithms based on the path-conservative central-upwind scheme, *J. Sci. Comput.* 89 (2021) 48, 24 pp.
- [14] A. Chertock, M. Herty, Ş.N. Özcan, Well-balanced central-upwind schemes for  $2 \times 2$  systems of balance laws, in: C. Klingenberg, M. Westdickenberg (Eds.), *Theory, Numerics and Applications of Hyperbolic Problems I*, in: *Springer Proc. Math. Stat.*, vol. 236, Springer, Cham, 2018, pp. 345–361.
- [15] A. Chertock, S. Karni, A. Kurganov, Interface tracking method for compressible multifluids, *M2AN Math. Model. Numer. Anal.* 42 (2008) 991–1019.
- [16] A. Chertock, A. Kurganov, Y. Liu, Central-upwind schemes for the system of shallow water equations with horizontal temperature gradients, *Numer. Math.* 127 (2014) 595–639.
- [17] S. Chu, A. Kurganov, R. Xin, A well-balanced fifth-order A-WENO scheme based on flux globalization, *Beijing J. Pure Appl. Math.* (2024), preprint available at <https://sites.google.com/view/alexander-kurganov/publications?authuser=0>.
- [18] S. Chu, A. Kurganov, R. Xin, Low-dissipation central-upwind schemes for compressible multifluids, *J. Comput. Phys.* 518 (2024) 113311, 35 pp.
- [19] G. Dal Maso, P.G. Lefloch, F. Murat, Definition and weak stability of nonconservative products, *J. Math. Pures Appl.* 74 (1995) 483–548.

- [20] D. Donat, A. Martinez-Gavara, Hybrid second order schemes for scalar balance laws, *J. Sci. Comput.* 48 (2011) 52–69.
- [21] L. Gascón, J.M. Corderán, Construction of second-order TVD schemes for nonhomogeneous hyperbolic conservation laws, *J. Comput. Phys.* 172 (2001) 261–297.
- [22] S. Gottlieb, D. Ketcheson, C.-W. Shu, *Strong Stability Preserving Runge-Kutta and Multistep Time Discretizations*, World Scientific Publishing Co. Pte. Ltd., Hackensack, NJ, 2011.
- [23] S. Gottlieb, C.-W. Shu, E. Tadmor, Strong stability-preserving high-order time discretization methods, *SIAM Rev.* 43 (2001) 89–112.
- [24] J.-F. Haas, B. Sturtevant, Interaction of weak shock waves with cylindrical and spherical gas inhomogeneities, *J. Fluid Mech.* 181 (1987) 41–76.
- [25] A. Kurganov, C.-T. Lin, On the reduction of numerical dissipation in central-upwind schemes, *Commun. Comput. Phys.* 2 (2007) 141–163.
- [26] A. Kurganov, Y. Liu, R. Xin, Well-balanced path-conservative central-upwind schemes based on flux globalization, *J. Comput. Phys.* 474 (2023) 111773, 32 pp.
- [27] A. Kurganov, Y. Liu, V. Zeitlin, Thermal versus isothermal rotating shallow water equations: comparison of dynamical processes by simulations with a novel well-balanced central-upwind scheme, *Geophys. Astrophys. Fluid Dyn.* 115 (2021) 125–154.
- [28] A. Kurganov, S. Noelle, G. Petrova, Semidiscrete central-upwind schemes for hyperbolic conservation laws and Hamilton-Jacobi equations, *SIAM J. Sci. Comput.* 23 (2001) 707–740.
- [29] A. Kurganov, E. Tadmor, New high-resolution semi-discrete central schemes for Hamilton-Jacobi equations, *J. Comput. Phys.* 160 (2000) 720–742.
- [30] Philippe G. LeFloch, *Hyperbolic systems of conservation laws*, in: *The Theory of Classical and Nonclassical Shock Waves*, in: *Lectures in Mathematics ETH Zürich*, Birkhäuser Verlag, Basel, 2002.
- [31] P.G. Lefloch, Graph solutions of nonlinear hyperbolic systems, *J. Hyperbolic Differ. Equ.* 1 (2004) 643–689.
- [32] K.-A. Lie, S. Noelle, On the artificial compression method for second-order nonoscillatory central difference schemes for systems of conservation laws, *SIAM J. Sci. Comput.* 24 (2003) 1157–1174.
- [33] A. Martinez-Gavara, R. Donat, A hybrid second order scheme for shallow water flows, *J. Sci. Comput.* 48 (2011) 241–257.
- [34] H. Nessyahu, E. Tadmor, Nonoscillatory central differencing for hyperbolic conservation laws, *J. Comput. Phys.* 87 (1990) 408–463.
- [35] C. Parés, *Path-Conservative Numerical Methods for Nonconservative Hyperbolic Systems*, *Quad. Mat.*, Dept. Math., vol. 24, Seconda Univ. Napoli, Caserta, 2009.
- [36] E. Pimentel-García, M.J. Castro, C. Chalons, T. Morales de Luna, C. Parés, In-cell discontinuous reconstruction path-conservative methods for non conservative hyperbolic systems—second-order extension, *J. Comput. Phys.* 459 (2022) 111152, 35 pp.
- [37] J.J. Quirk, S. Karni, On the dynamics of a shock-bubble interaction, *J. Fluid Mech.* 318 (1996) 129–163.
- [38] K.A. Schneider, J.M. Gallardo, D.S. Balsara, B. Nkonga, C. Parés, Multidimensional approximate Riemann solvers for hyperbolic nonconservative systems. Applications to shallow water systems, *J. Comput. Phys.* 444 (2021) 110547, 49 pp.
- [39] K.-M. Shyue, An efficient shock-capturing algorithm for compressible multicomponent problems, *J. Comput. Phys.* 142 (1998) 208–242.
- [40] P.K. Sweby, High resolution schemes using flux limiters for hyperbolic conservation laws, *SIAM J. Numer. Anal.* 21 (1984) 995–1011.
- [41] L. Xu, T.G. Liu, Explicit interface treatments for compressible gas-liquid simulations, *Comput. Fluids* 153 (2017) 34–48.